Lawrence Berkeley National Laboratory
LBL Publications

Title
Metal-Supported Solid Oxide Electrolysis Cell with Significantly Enhanced Catalysis

Permalink
https://escholarship.org/uc/item/8p78804c

Journal
Energy Technology, 7(5)

ISSN
2194-4288

Authors
Wang, Ruofan
Dogdibegovic, Emir
Lau, Grace Y
et al.

Publication Date
2019-05-01

DOI
10.1002/ente.201801154

Peer reviewed

eScholarship.org Powered by the California Digital Library
University of California

DOI: 10.1002/ ((please add manuscript number))
Article type: Full Paper

Metal-Supported Solid Oxide Electrolysis Cell (MS-SOEC) With Significantly Enhanced Catalysis

*Ruofan Wang, Emir Dogdibegovic, Grace Y. Lau, Michael C. Tucker**

Dr. R. Wang, Dr. E. Dogdibegovic, G. Y. Lau, Dr. M. C. Tucker
Energy Storage and Distributed Resources Division
Lawrence Berkeley National Laboratory
1 Cyclotron Road, Berkeley, CA 94720, United States
E-mail: mctucker@lbl.gov

Keywords: solid oxide electrolysis, solid oxide electrolyzer cells, high temperature electrolysis, hydrogen production, infiltration

High temperature electrolysis (HTE) using solid oxide electrolysis cells (SOECs) is a promising hydrogen production technology and has attracted substantial research attention over the last decade. While most studies were conducted on hydrogen electrode-supported type cells, SOEC operation using metal-supported cells has received minimal attention. In this study, development of metal-supported solid oxide electrolysis cells with performance similar to the best conventional SOECs is reported. These cells have stainless steel supports on both sides, 10Sc1CeSZ electrolyte and electrode backbones, and nano-structured catalysts infiltrated on both hydrogen and oxygen electrode sides. Samarium doped ceria (SDC) mixed with Ni is infiltrated as hydrogen electrode catalyst, and the effect of ceria:Ni ratio is studied. On the oxygen electrode side, catalysts including lanthanum strontium manganite (LSM), lanthanum strontium cobalt ferrite (LSCF), praseodymium oxide (Pr_6O_{11}), and their composite catalysts with SDC (i.e. LSM-SDC, LSCF-SDC, and Pr_6O_{11}-SDC) are compared. By employing the materials with highest catalytic activity (Pr_6O_{11}-SDC and SDC40-Ni60) and optimizing the catalyst infiltration processes, excellent electrolysis performance of metal-supported cells is achieved. Current densities of -5.31, -4.09, -2.64, and -1.62 A cm^{-2} are achieved at 1.3 V and 50 vol.% steam content, at 800, 750, 700, and 650 °C, respectively.

1. Introduction

Hydrogen as an energy carrier has the highest energy-to-weight ratio, and therefore it has been advocated as the desired fuel for automotive power, auxiliary power, stationary power generation, and also as an energy storage medium. However, to realize the hydrogen economy, [1-3] hydrogen needs to be produced inexpensively and in an environmental-friendly manner. Currently, bulk hydrogen is most commonly produced by the steam reforming of methane or natural gas, but this process also generates unfavorable byproducts such as CO, CO_2 and other greenhouse gases.[4-7] In contrast, hydrogen production through water electrolysis is considered to be the cleanest method when renewable energy sources provide the electricity. [8-13]

Among various water electrolysis methods, high temperature electrolysis (HTE) using solid oxide electrolysis cells (SOECs) has attracted substantial attention over the last decade due to high efficiency of conversion and low energy consumption [9, 14-20]. A solid oxide electrolysis cell is essentially a solid oxide fuel cell operating in reverse, using electricity to split water molecules in steam into hydrogen and oxygen. Such a device is usually operated in the relatively high temperature range of 700 to 900 °C, thus resulting in a high conversion efficiency, because (a) a significant part of the required energy can be provided by external heat for an ideal HTE, and (b) the electrode reaction kinetics are faster at higher temperatures [13, 21]. To date, extensive effort has been devoted to the development of highly efficient SOECs and promising results have been shown [15, 22-39].

SOECs are also proposed to be used as buffers for intermittent renewable sources (such as wind power and nuclear power) by utilizing surplus electricity and waste heat [25, 40]. From

the intermittent operating point of view, however, conventional all-ceramic cell structures may not be ideal due to low tolerance for redox cycling and thermal cycling. Instead, metal-supported solid oxide cells (MS-SOCs) that incorporate a porous ferritic steel as substrate could become a potential solution for intermittent applications, primarily due to their unique advantages of good redox stability and excellent thermal cycling resistance [41-43]. Advantages of metal-supported cells over conventional all-ceramic cells also include low-cost structural materials (stainless steels) and mechanical ruggedness, showing great promise of MS-SOCs for mobile and/or intermittent application. In recent years, substantial development of metal-supported fuel cells (MS-SOFCs) has resulted in excellent performance and durability, and demonstration of the unique advantages discussed above [44-69]. Our group has developed symmetric structure MS-SOFC with infiltrated catalysts on both electrodes, and demonstrated high performance [47], rapid thermal-cycling [48, 49] and dynamic-temperature operation of the cells [47, 48, 50]. Nielsen et al. from Technical University of Denmark adopted a relatively thin metal support with thickness of 175 μm and demonstrated high cell performance [58]. Long-term stack operation of MS-SOFCs has been demonstrated by Topsoe [70] and Ceres [71]. Details of the progress of MS-SOFCs can be read in review papers Ref. [41], Ref. [42], and Ref [43].

Despite the high level of development of MS-SOFCs, only a few initial assessments of MS-SOEC operation are available [18, 72, 73]. For example, Schiller et al. from DLR reported high temperature electrolysis using a metal-supported cell for the first time, with Ni/8YSZ hydrogen electrode and LSM oxygen electrode providing a cell voltage of about 1.4 V at current density of –1.0 A cm^{-2} at 800 °C and 30 vol.% H_2O-H_2 [18]. Chen et al. from SICCAS used a MS-SOEC with impregnated Ni-SDC and Nd_2O_3-NNO catalysts and demonstrated a comparable performance with state-of-the-art all-ceramic SOECs [73]. These efforts clearly demonstrate the potential of using metal-supported cells for high temperature electrolysis,

which motivates us to adapt and optimize the MS-SOFCs developed at LBNL for electrolysis operation.

In this work, MS-SOCs with stabilized zirconia electrolyte were used for the development of high electrolysis performance. The symmetric cell structure with co-sintered porous backbones and metal supports, and infiltrated electrocatalysts on both steam and oxygen electrodes, enables straightforward comparison of the electrochemical activities of various catalyst materials without changing the sintering protocol, and provides the opportunity to optimize the catalyst microstructure deposited via infiltration. The cells were tested in the temperature range from 650 to 800 °C, with steam content between 3-75 vol.%. Our MS-SOECs show excellent performance: at 1.3 V (near thermoneutral voltage) and 50 vol.% steam content, the measured current densities were -5.31 A cm^{-2} at 800 °C, -4.09 A cm^{-2} at 750 °C, -2.64 A cm^{-2} at 700 °C, and -1.62 A cm^{-2} at 650 °C. This performance was achieved by optimizing the catalyst compositions, catalyst arrangement, and infiltration process. In order to elucidate the impact of the catalyst fabrication process, the electrochemical performance at various steam contents and overpotentials was analyzed with electrochemical impedance spectroscopy (EIS) and distribution of relaxation times (DRT), and the corresponding microstructures were examined. The high cell performance indicates great potential of MS-SOEC technology, and the insight from these experiments will provide guidance for further research and development.

2. Results and Discussion

2.1. Cell Microstructure

Metal-supported cells used in this study have a symmetric structure: a dense 10Sc1CeSZ (scandia-ceria-stabilized zirconia, SCSZ) electrolyte layer is sandwiched in between porous

SCSZ backbone layers, with porous stainless steel substrate on both sides, **Figure 1a-c**. The thicknesses of the porous metal support, porous SCSZ electrode backbone, and dense SCSZ electrolyte are approximately 180, 15, and 10 μm, respectively, Figure 1b-c. The porosities of the metal-support and backbone are approximately 30% and 43%. The adequate porosity of the metal and ceramic layers enables catalysts infiltration throughout the cell structure without catalyst clogging, and without sacrificing mechanical ruggedness of the cell. By infiltrating catalysts using nitrate precursors with sequential calcination steps, continuous blankets of catalyst were formed on the interior surface of the SCSZ backbone. Figure 1d and 1e shows the scanning electron microscopy (SEM) images of the representative $Sm_{0.2}Ce_{0.8}O_{2-\delta}$ (SDC) mixed with 20 vol.% Ni (SDCN20) as fuel electrode catalyst and Pr_6O_{11} as oxygen electrode catalyst in the fractured porous SCSZ backbone. The thickness of the infiltrated layers is approximately 100-200 nm. The primary catalyst size is approximately 30 nm for SDCN20 and 20 nm for Pr_6O_{11}.

2.2. Effect of Oxygen Electrode Catalyst

As a starting point, cells with a single catalyst $La_{0.15}Sr_{0.85}MnO_{3-\delta}$ (LSM), $La_{0.6}Sr_{0.4}Co_{0.2}Fe_{0.8}O_{3-\delta}$ (LSCF), or Pr_6O_{11} [74-77] on the oxygen electrode side and $Sm_{0.2}Ce_{0.8}O_{2-\delta}$ (SDC) mixed with 20 vol.% Ni (SDCN20) on the hydrogen electrode side were fabricated. Three infiltration cycles were used for both oxygen and hydrogen electrodes. X-ray diffraction confirmed that the correct LSM, LSCF, Pr_6O_{11}, and SDC-Ni catalyst phases were formed, see Figure S1. Additional minor Fe_3O_4 impurity phase was found in the case of LSCF. The fuel cell and electrolysis performance of these cells at 700 °C with 50 vol.% absolute humidity (AH) in hydrogen is highest for Pr_6O_{11} and lowest for LSM, Figure 2a. At 1.3 V cell voltage, the current densities for LSM, LSCF, and Pr_6O_{11} were -0.80, -0.92, and -1.13 A cm^{-2}, respectively. EIS was used to separate ohmic and polarization impedances, and

elucidate differences between the catalyst compositions, Figure 2b-c. At open-circuit voltage (OCV), the ohmic resistance with LSM, LSCF, and Pr_6O_{11} was 0.096, 0.127, and 0.120 $\Omega \cdot cm^2$, respectively, and the polarization resistance (R_p) was 0.58, 0.31, and 0.21 $\Omega \cdot cm^2$, respectively. Although LSM provides lower ohmic resistance, its high polarization resistance dominates catalytic activity near OCV. In contrast, Pr_6O_{11} and LSCF provided relatively smaller polarization resistance and slightly higher ohmic resistance. Under +0.2 V DC bias (i.e. electrolysis mode), the ohmic resistances of LSM, LSCF, and Pr_6O_{11} based cells were similar to those measured at OCV, but their polarization resistances improved to 0.31, 0.24, and 0.18 $\Omega \cdot cm^2$, respectively. Smaller R_p values at +0.2 V illustrates that the electrolysis reaction is promoted by the positive DC bias when a large amount of reactant (high steam content) is provided for electrolysis. In contrast, R_p measured at OCV represents polarization resistance under cell equilibrium, thus high steam content in hydrogen will cause mass transfer limitation when AC potential is shifted to negative values (i.e. in SOFC mode). As will be shown in the rest of the paper, area specific resistance (ASR) of the cell typically increases when cell voltage decreases from OCV, due to the high fuel utilization condition (high steam content). For cells with LSM, LSCF, and Pr_6O_{11} catalysts, the ASR's measured from V-i curves at OCV + 0.2 V were 0.37, 0.31, and 0.28 $\Omega \cdot cm^2$, respectively, consistent with total impedance measured at + 0.2 V.

2.3. Oxygen Electrode with Doped Ceria Composite Improves Performance

Although LSCF and Pr_6O_{11} are considered to have mixed ionic and electronic conductivities, the electronic contribution dominates [76, 78]. Incorporation of an ionic conductor (such as doped ceria) into the oxygen electrode is a common approach to increase the triple-phase boundary length available for the oxygen reduction reaction (ORR) in SOFC cathodes [79-83]

or oxygen evolution reaction (OER) in SOEC anodes [84, 85]. Here, samaria-doped ceria (SDC) was added to the oxygen electrode via infiltration as a second separate layer, i.e. an "ABAA" layered arrangement was obtained, where "A" stands for electronic conductor LSM, LSCF, or Pr_6O_{11}, and "B" stands for ionic conductor SDC (such denotations will be used in this paper for ease of expressing the infiltration steps).

Addition of SDC to form a composite catalyst significantly improved performance for all oxygen catalysts studied, Fig. 3a. At 1.3 V, cells with LSM-SDC, LSCF-SDC and Pr_6O_{11}-SDC composite electrode provided current densities of -0.94, -1.16, and -1.93 A cm^{-2}, respectively, resulting in 18%, 26% and 71% improvement compared to the corresponding single catalyst electrodes. It appeared that SDC provided higher improvement for materials with higher catalytic activity. EIS reveals improvement primarily to the polarization resistance upon addition of SDC, Fig. 3b-d. The ohmic resistance (R_Ω) of LSM-SDC, LSCF-SDC, and Pr_6O_{11}-SDC cells was 0.101, 0.112, and 0.088 $\Omega \cdot cm^2$, respectively, and the polarization resistance (R_p) was 0.19, 0.17, and 0.09 $\Omega \cdot cm^2$, respectively. Interestingly, for LSCF and Pr_6O_{11} catalysts, addition of SDC also decreased the ohmic resistance, Fig. 3c-d. The decrease of both R_p and R_Ω suggests that incorporating SDC into oxygen electrode enhances the three phase boundaries (TPB's) for oxygen evolution reaction, and also improves ionic conduction in the infiltrated layers.

2.4. Enhanced OER Catalysis with Alternating-Infiltrated Composite Electrode

As described in Section 2.3, by incorporating SDC in the oxygen electrode, the cell performance can be significantly improved. To determine which electrode dominates the cell polarization, symmetric cells with LSCF-SDC, Pr_6O_{11}-SDC, or SDCN20 infiltrated in both electrodes and measuring their impedance spectra in the relevant atmospheres at OCV, Fig.

S2. It was found that the polarization resistance of the oxygen electrode (LSCF-SDC or Pr_6O_{11}-SDC) was significantly higher than that of hydrogen electrode (SDCN20), which implies R_p from oxygen electrode dominates total cell resistance. Further details are provided in Supplementary Note 1.

With the intention to enhance OER activity of the oxygen electrode, various infiltration strategies for fabricating the composite oxygen electrode were implemented. Here, Pr_6O_{11}-SDC composite catalyst was used for this study as it provided the highest cell performance, as discussed in Section 2.3. Three sequences of composite electrode infiltrations were compared, namely "ABAA", "ABABA", and "AB mixture + A", where "A" represents the electronic conductor (Pr_6O_{11} in this case), and "B" represents the ionic conductor (SDC in this case). The expected schematics of catalyst arrangements in the porous backbone are shown in Fig. 4a, and their infiltration processes are described in detail as follows:

(a) ABAA (as baseline): The first layers of Pr_6O_{11} and SDC are infiltrated separately and each fired at 850 °C so that a good electronic pathway from Pr_6O_{11} and good extension of ionic conduction from SDC can be obtained. On top of the first two layers, two more layers of Pr_6O_{11} are infiltrated and fired at 600 °C to provide a higher surface area for oxygen evolution.

(b) ABABA: Compared with ABAA, this alternating-layer composite arrangement includes an additional layer of SDC between the last two layers of Pr_6O_{11}, fired at 600 °C. The additional SDC layer is intended to extend the ionic conduction network and to create more TPB throughout the thickness of the catalyst layers.

(c) AB mixture + A: In contrast to the other two sequential arrangements, nitrate salts precursors for Pr_6O_{11} and SDC were mixed in a single solution yielding a final volume ratio of Pr_6O_{11}:SDC = 1:1. This mixed-nitrate solution was infiltrated into the porous backbone twice (fired at 850 and 600 °C, respectively), followed by one additional

Pr_6O_{11}. The Pr_6O_{11} and SDC mixture is intended to create intimate mixing of electronic and ionic conduction pathways, providing a true "composite" electrode. XRD of the mixed Pr_6O_{11}-SDC confirmed that secondary non-fluorite phases were not formed, Fig. S3.

The sequence of composite catalyst deposition significantly impacts electrolysis performance, Fig. 4b. At 1.3 V, "ABABA", "ABAA", and "AB mixture + A" cells provided -1.91, -1.50, and -1.19 A cm^{-2} current densities, respectively. EIS indicates this trend is related to improvements in both the ohmic and polarization resistances, Fig. 4c-d. Comparison of Bode plots of the three cells clearly shows that the major advancement provided by the ABABA configuration was due to the decrease of impedance at higher frequencies at ~10^2 to 10^4 Hz, whereas the impedances at lower frequencies (less than 10 Hz) were about the same.

To further understand the sensitivity of the oxygen electrode performance to infiltration sequence, distribution of relaxation times (DRT) analysis was performed so that different electrode physical/chemical processes could be isolated in their corresponding frequency domain [86, 87]. DRT method has been widely used for analyzing performance of SOEC with Ni-YSZ hydrogen electrode [88-90], and was also recently adopted for cells with Ni-GDC or Ni-YSZ-GDC electrode with both metal-supported and ceramic-supported structures [56, 58, 91-93]. An open-source program "DRTTOOLS" with Tikhonov Regularization method is used here [94, 95]. Unlike Bode or Nyquist plots where different processes overlap, at least four processes (i.e. four distinct peaks denoted as P_1, P_2, P_3 and P_4) can be identified in the DRT plots, Fig. 5. The physical meanings of these processes are summarized as follows:

- P_4 (10^{-1} – 10 Hz): It is generally agreed that the process giving rise to this peak is dominated by the gas diffusion in both oxygen electrode [87, 93] and hydrogen electrode

[44, 96, 97]. This peak shrinks drastically with increasing steam content (Fig. S4) in the hydrogen electrode but is independent of temperature (Fig. S8), supporting its assignment to a gas diffusion/mass transfer process.

- P_3 (1 - 10^2 Hz): These peaks are of similar size for different infiltration sequences at OCV, and decrease as the absolute operating current density increases. Previous studies have shown that the related process is sensitive to H_2O content [87, 96], and we assign P_3 to steam-hydrogen conversion in the hydrogen electrode. P_3 also diminished when the cell was operated under electrolysis mode (+0.2 V) but was amplified under fuel cell condition (-0.2 V), indicating steam-to-hydrogen conversion is more favorable than hydrogen-to-steam conversion under this specific testing condition (50 vol.% H_2O, 700 °C), Fig. S9.
- P_2 (10^2 - 10^3 Hz): For symmetric cells, this peak is pronounced for the oxygen electrode, but vanished for the hydrogen electrode, Fig. S2a. P_2 decreases with increasing temperature (Fig. S8), but is almost independent of steam content (Fig. S4) and cell operating voltage (Fig. S9). These observations are in good agreement with previous studies that assign this intermediate frequency peak to oxygen surface exchange and O^{2-} bulk diffusion [93, 96, 98].
- P_1 (10^3 - 10^4 Hz): The high frequency process is strongly temperature dependent (Fig. S8) and also highly sensitive to oxygen electrode composition (Fig. 4c-d). From symmetric cell testing, it was evident that this process is pronounced in both oxygen and hydrogen electrodes (Fig. S2a). Therefore, P_1 is assigned to charge transfer across electrode/electrolyte interfaces in both electrodes [87, 93].

Comparing DRT spectra at OCV (Fig. 5a) and under electrolysis condition at +0.2 V (Fig. 5b), similar P_1 and P_2 peak sizes were observed for individual cells, indicating that charge transfer and oxygen exchange/diffusion processes are insensitive to operating voltage. P_3 and P_4 peak

heights, however, were significantly lower under electrolysis condition (Fig. 5b) than open-circuit condition (Fig. 5a), consistent with mass transfer or steam-hydrogen conversion. Using DRT, Fig. 5 clearly shows that the improvement of cell performance with alternating-layer infiltrated composite electrode (ABABA) was primarily due to the decrease of P_2 and P_1. This suggests that both charge transfer and oxygen surface exchange/bulk diffusion processes were enhanced by optimizing the infiltration approach for the composite oxygen electrode.

The microstructure of the alternating-layer (ABABA) infiltrated Pr_6O_{11}-SDC composite catalyst is shown in Fig. 6. Two representative regions are enlarged in Fig. 6b and Fig. 6c, and they can be described as follows:

- Intimately mixed Pr_6O_{11} and SDC catalysts are observed on the surface of the SCSZ backbone, Fig. 6b. Two catalysts with different sizes can be observed: small catalysts with particle size of ~20-30 nm and larger catalysts that are embedded under the small catalysts having size of ~100-150 nm. The energy X-ray dispersive spectroscopy (EDS) spectrum obtained from a large catalyst covered by small particles (Fig. 6d) reveals that both Pr_6O_{11} and SDC catalysts are present with a larger atom% of Ce than Pr, indicating that the larger covered particles are SDC and the smaller particles are Pr_6O_{11}.
- Pure Pr_6O_{11} catalyst that is extended away from the SCSZ surface, Fig. 6c. Dendritic-like nano-catalyst structure with homogenous particle size of ~ 20-30 nm was observed. EDS spectrum obtained from the same area (Fig. 6e) confirmed that the small particles are Pr_6O_{11}. We presume that this is the last layer of catalyst deposited during infiltration.

Based on the EIS/DRT analysis and the microstructure of the infiltrated catalysts, plausible reasons for enhanced performance of Pr_6O_{11}-SDC ABABA composite electrode can be inferred:

(a) The SDC catalysts with the size of ~100 nm, which are covered by small Pr_6O_{11} particles, appeared to form connected “mountains” next to the surface of SCSZ (Fig. 6b). Thus, in addition to the Pr_6O_{11}/backbone (SCSZ) interface, the TPB (i.e. Pr_6O_{11}/SDC/O_2 three phase boundary) is extended into the catalyst layer thickness, resulting in much larger area for the charge transfer reaction.

(b) By infiltrating Pr_6O_{11} and SDC in an alternating-layer composite sequence, a complex mixed electronic and ionic conduction network was created, resulting in higher density of O^{2-} diffusion pathways and oxygen surface exchange sites for OER.

(c) The additional SDC improves ionic conduction in the electrode, resulting in decreased ohmic resistance.

We also investigated the effect of further infiltration of electronic conductor on top of ABABA arrangement. Fig. S5 shows that for both LSCF-SDC and Pr_6O_{11}-SDC cells, an additional two infiltration layers of LSCF or Pr_6O_{11} resulted in increased gas diffusion limitation due to pore clogging, and therefore was determined to be non-optimal. Details of the effect of over-filling the oxygen electrode with catalyst on cell performance can be seen in Fig. S5 and Supplementary Note 2.

Overall, the alternating-layer catalyst arrangement was determined to be the preferred infiltration strategy for the Pr_6O_{11}-SDC composite electrode operating in electrolysis mode. This strategy was also applied to the LSCF-SDC composite electrode and similarly improved the cell performance, Figs S6, S7, and S10. We anticipate that this alternating-layer composite infiltration strategy will also enhance performance of other catalyst materials.

2.5. Optimizing Hydrogen Electrode Catalyst Ceria:Ni Ratio

Ni-SDC cermet is widely used as the steam/hydrogen electrode in solid oxide electrolysis cells, and Ni-SDC infiltration is common in metal-supported cells. To further optimize the cell performance, we investigated the effect of ceria:Ni volume ratio in the infiltrated electrode on electrolysis performance, Fig. 7. At 1.3 V, cells with 20, 40, and 60 vol.% Ni in Ni-SDC (denoted as SDCN20, SDCN40 and SDCN60) provided 1.50, 1.70, and 2.00 A cm^{-2}, respectively. The ASR measured from V-i curves at OCV + 0.2 V was 0.21, 0.19, and 0.16 $\Omega \cdot cm^2$, respectively. To elucidate the role of higher Ni content in improving cell performance, impedance spectra of cells with 20 vol.% and 60 vol.% Ni contents are compared, Fig. 7b. It was found that R_p of the cell with 60 vol.% Ni was 0.088 $\Omega \cdot cm^2$, which was almost identical to that of the cell with 20 vol.% Ni. The Bode spectra are nearly identical, indicating that variation of Ni content does not affect the electrode reaction kinetics. Higher Ni content does however result in a smaller ohmic resistance: R_Ω was 0.088 $\Omega \cdot cm^2$ for 20 vol.% Ni but was 0.064 $\Omega \cdot cm^2$ for 60 vol.% Ni. Thus, it is considered that higher Ni content increases electronic percolation in Ni-SDC infiltrated hydrogen electrode.

2.6. Performance of Optimized Cells

By aggregating the oxygen and hydrogen electrode catalyst materials and infiltration process optimizations into a single improved cell, excellent cell performance was obtained, Fig. 8a-b. Specifically, the hydrogen catalyst was SDCN60, and the oxygen catalyst was Pr_6O_{11}-SDC deposited via the ABABA infiltration sequence. The cell shows concentration polarization at 3 vol.% H_2O due to the insufficient steam supply, but the V-i curves with steam content of 25 vol.% and higher were almost linear. At 1.3 V and 700 °C, the current density of the cell at 3, 25, 50, and 75 vol.% H_2O was -0.63, -2.27, -2.64, and -3.48 A cm^{-2}, respectively, Fig. 8a. The

cell displays smaller polarization resistance in electrolysis mode (0.054 $\Omega \cdot cm^2$ at OCV + 0.2 V) than OCV (0.075 $\Omega \cdot cm^2$) and fuel cell mode (0.172 $\Omega \cdot cm^2$ at OCV - 0.2 V), at 50 vol.% H_2O as example, Fig. S9. Detailed impedance spectra of the optimized cell as functions of temperature and operating voltage are provided as Fig. S8 and Fig. S9.

The optimized cell performance was also characterized as a function of temperature, Fig. 8b. At 1.3 V with 50 vol.% steam content, current density of -5.31, -4.09, -2.64, and -1.62 A cm^{-2} was obtained at 800, 750, 700, and 650 °C, respectively. Assuming 100% current efficiency, steam-to-hydrogen conversion rate (SC) at this operating condition is calculated to be 96%, 74%, 48%, and 29% at 800, 750, 700, and 650 °C, respectively (using Faraday's law) [17, 31, 99]. The details of the calculation of hydrogen production rate and steam-to-hydrogen conversion rate (SC) are provided in the Supplementary Note 3 and Table S1. The ASR measured from the slope of the V-i curves at OCV + 0.2 V was 0.07, 0.09, 0.13 and 0.20 $\Omega \cdot cm^2$, at 800, 750, 700, and 650 °C, respectively.

The catalyst compositions and infiltration process in this study are optimized for SOEC operation, and are different from the those for optimized MS-SOFC [100]. It is clearly demonstrated that MS-SOC with symmetric cell structure is flexible for both electrolysis and fuel cell operation, i.e., strong performance improvements can be achieved by substantial catalyst optimization without re-optimizing cell architecture or sintering protocols.

Fig. 8c compares the electrolysis performance of our optimized cells with those of oxygen-conducting SOECs reported in the literature. Some recent advances of electrolysis cells based on proton conductors (such as [29, 101-103]) are not shown here, as the operating temperatures (400-600 °C) and steam contents (up to 10 vol.%) reported for these proton-

conducting SOECs are very different from the ones based on conventional oxygen conductors (700-900 °C, 50 vol.% or higher steam content). The cell with Pr_6O_{11}-SDC oxygen electrode achieved very high electrolysis performance, surpassing conventional electrode-supported cells and all previous metal-supported electrolysis cells. Also shown in Fig. 8c is performance with LSCF-SDC catalyst (electrochemical characteristics are provided in Fig. S10), which is comparable to state-of-the-art electrolysis cells, clearly demonstrating that metal-supported cells can achieve excellent electrolysis performance with commonly-used electrode materials.

3. Conclusion

In this work, symmetric-structure metal-supported solid oxide electrolysis cells are developed for high temperature electrolysis. Various nanoscale catalyst materials and compositions were infiltrated for both oxygen and hydrogen electrodes. Pr_6O_{11} was found to be an improved OER catalyst material, compared to LSCF and LSM. By incorporating SDC in the oxygen electrode to form a composite with Pr_6O_{11}, LSCF, or LSM, cell performance was substantially improved, with Pr_6O_{11}-SDC providing the highest catalytic activity. On the hydrogen electrode side, ceria:Ni volume ratios from 80:20 to 40:60 were compared. It was found increasing Ni content in the hydrogen electrode significantly decreases the ohmic resistance, while not impacting the polarization resistance significantly. In order to further reduce the polarization resistance of the cell (especially the dominant oxygen electrode resistance), different infiltration strategies for the composite oxygen electrode catalyst were investigated, and found to significantly impact performance. An alternating-layered infiltration sequence of catalyst and SDC was identified to be optimal, providing the lowest ohmic and polarization resistances. It was found that cell performance was most sensitive to SDC incorporation and infiltration sequence at the oxygen electrode, due to the significantly improved charge transfer and oxygen surface exchange/diffusion for OER.

By aggregating the oxygen and hydrogen electrode catalyst materials and infiltration process optimizations into a single improved cell, very high cell performance was obtained. Without changing the sintered cell structure, the cell current density was improved from -0.80 A cm^{-2} (baseline LSM/SDCN20) to -2.64 A cm^{-2} (Pr_6O_{11}-SDC/SDCN60) with ASR reduced from 0.37 $\Omega \cdot cm^2$ to 0.13 $\Omega \cdot cm^2$, at 1.3 V, 50 vol.% H_2O, and 700 °C. For an optimized cell with a Pr_6O_{11}-SDC composite oxygen electrode and a $Sm_{0.2}Ce_{0.8}O_{2-\delta}$ mixed with Ni (i.e. SDCN) hydrogen electrode, current density of -5.31, -4.09, -2.64, and -1.62 A cm^{-2} was obtained at 800, 750, 700, and 650 °C, respectively, at 1.3 V and 50 vol.% steam content. To the best of our knowledge, this excellent MS-SOEC performance is among the highest reported to date for any type of oxygen-conducting SOEC.

Due to the unique characteristics of metal-supported cells including their low manufacturing cost, excellent redox cycling and thermal cycling tolerance, and fast start-up capability, the high-performance MS-SOECs developed in this study are considered to have high potential for certain novel applications, such as buffering intermittent excess electricity and heat from renewable energy, and hydrogen production for mobile applications. Upcoming research will focus on durability and degradation of these MS-SOECs, and will be reported in the future.

4. Experimental Section

Metal-Supported Cell Fabrication: Metal-supported cells used in this study were prepared by a co-sintering fabrication process. SCSZ (DKKK, Japan) and stainless steel (P434L alloy, water atomized, Ametek Specialty Metal Products) layers were prepared by tape casting, using polymethyl methacrylate pore-former beads (Esprix Technologies) and water-based tape-casting binder. After tape casting, these layers were then laminated into a green cell

assembly with aforementioned cell architecture. Individual cells were cut into circular shapes (with diameter of 30 mm) from a large green sheet with a laser cutter (Hobby model, Full Spectrum Laser). These circular cells were fired in air in a muffle furnace at 525 °C for 1 h to remove the binder and pore former. Cells were then sintered at 1350 °C for 2 h in a tube furnace with 2% H_2 – Ar flowing inside, in order to obtain a dense SCSZ electrolyte and also mechanically rugged porous metal supports with high electronic conductivity.

After co-sintering of the metal and ceramic layers, electrode catalysts were introduced into the porous SCSZ backbones on both oxygen and hydrogen electrode sides by infiltrating precursor solutions of nitrate salts [45, 47, 104]. In this work, six types of oxygen evolution catalysts were fabricated and studied: single catalysts including $La_{0.15}Sr_{0.85}MnO_{3-\delta}$ (LSM), $La_{0.6}Sr_{0.4}Co_{0.2}Fe_{0.8}O_{3-\delta}$ (LSCF), Pr_6O_{11}, and composite catalysts with $Sm_{0.2}Ce_{0.8}O_{2-\delta}$ (SDC) including LSM-SDC, LSCF-SDC, and Pr_6O_{11}-SDC (with catalyst-SDC ratios determined by the number of individual infiltration steps as discussed in Section 2.4). On the steam side of the cells, $Sm_{0.2}Ce_{0.8}O_{2-\delta}$ (SDC) mixed with Ni (SDCN) was used as hydrogen electrode catalyst. The ceria:Ni volume ratio was varied as 80:20, 60:40, or 40:60 (corresponding electrodes are denoted as SDCN20, SDCN40, and SDCN60).

Precursors solutions for infiltration were prepared by dissolving metal nitrates (Sigma-Aldrich) with intended stoichiometric ratio into a mixture of surfactant (Triton-X 100, Sigma-Aldrich) and distilled water (surfactant-water mixture was prepared by stirring for 1 h at room temperature). Surfactant loading was 0.3 g per 2 g of resulting catalyst particles, and final water/solution ratio was 15-40 wt.%, intended to improve wettability of precursor solution into pores of ceramic backbone. Before infiltration, the precursor mixture was stirred and heated at 50 – 60 °C on a hot plate for 30 min to completely dissolve the metal nitrate. Infiltration of precursor solutions were then performed by submerging the cells into the

precursor solutions at approximately 90 °C, with mild vacuum (~500 mbar) applied to evacuate the air in the cell pores. To avoid infiltration of precursor solutions into unintended area, the cells were masked with acrylic paint (Liquitex) with only the desired active area exposed. The active area of a cell was 1 cm^2.

After infiltrating the precursor, the cells were then fired at 850 or 600 °C (discussed further below) for 30 min in air in a muffle furnace to convert the metal nitrates into the desired oxide phases. Any loose catalyst on the surface of the cells after firing was removed by light brushing. Cells were re-infiltrated for a number of times, until the desired catalyst loading was achieved. The volume of catalyst introduced by each infiltration cycle can be estimated from the concentration of precursor solution and catalyst density, assuming the pores are completely flooded with precursor solution. Thus, catalyst loading per infiltration cycle can be represented by the filling factor, which is volume fraction of catalyst in the pores. The filling factors per infiltration cycle for LSM, LSCF and Pr_6O_{11} are all in the range of 5-7%, and those for Ni and SDC are approximately 3% and 10%, respectively. Some details of infiltration cycles can be described as follows:

a. Hydrogen electrode catalyst: For different ceria:Ni ratio, the number of infiltrations was varied until a final Ni filling factor of 8% was obtained. Based on our previous SOFC work, performance of cells plateaued around this Ni loading and further infiltration cycles would not increase the cell performance significantly [47].
b. Single oxygen electrode catalyst: Single oxygen electrode catalysts (LSM, LSCF, or Pr_6O_{11}) were infiltrated for three times, as it was found in our previous study that performance of cells with three infiltration cycles of LSM in oxygen electrode was optimal for SOFC operation [47]. The corresponding catalyst filling factor was approximately 11%.

c. Composite oxygen electrode catalyst: Two infiltration strategies were used for the composite catalyst: (a) infiltration of a solution which is mixture of precursor nitrates for both the electronic conductor (LSM, LSCF, or Pr_6O_{11}) and the ionic conductor (SDC), and (b) introduction of the electronic and ionic conductors separately in different infiltration cycles. Details of composite oxygen electrode infiltration are also described in Section 2.4.

d. Crystallization temperature of infiltration cycles: The crystallization temperature of each infiltration cycle was either 850 or 600 °C. The first infiltrated layer of any catalysts (LSM/LSCF/Pr_6O_{11}/SDC/SDCN) was fired at 850 °C to improve the percolation of particles, which can result in improved electronic conductivity of the electrode. The subsequent infiltrated catalyst layers were fired at 600 °C in order to provide high surface area of electrodes [47].

Electrochemical Testing: After a full cell was fabricated, platinum mesh was spot-welded on each side of the cell and two nickel-chromium alloy wires were spot-welded on each platinum mesh as current lead and voltage probe. Cells were then mounted on 410 stainless steel test rigs using glass paste (GM31107, Schott). Cells were heated at 2 °C/min to 200 °C to remove glass ink vehicle (Terpineol, Fuel Cell Materials) and then at 10 °C/min to 700 °C for 1 h to cure the glass sealant in ambient air. After curing of glass paste, the chamber on the hydrogen electrode side was flushed with nitrogen and then hydrogen bubbled though water at room temperature with flow rate of 100 cm^3/min. Open-circuit voltage (OCV) was measured to confirm the leak-tightness of the cell and test rig.

After OCV of the cell was established and NiO on the hydrogen electrode side was completely reduced to Ni, cell performance was characterized by voltage-current density (V-i)

curves and electrochemical impedance spectroscopy (EIS). For SOEC testing, hydrogen was used as the carrier gas in the hydrogen electrode to control the steam content. Hydrogen flow rate was controlled at 50 cm^3/min by mass flow controller (MKS). Hydrogen was bubbled through a water bath with temperature maintained at ~25, 65, 82, and 92 °C to control the absolute humidity (AH, i.e. the vol.% humidity in the total gas) at 3, 25, 50, and 75 vol.% AH, respectively. Stainless steel flexible tubing (Swagelok) was used downstream of the water bubbler and heated above 100 °C with heating tape to avoid steam condensation before the testing furnace. During cell testing, the oxygen electrode was always exposed to stagnant ambient air. Cells were tested with various steam contents (3, 25, 50, and 75 vol.% AH) and at different temperatures (650, 700, 750, and 800 °C) under both electrolysis and fuel cell modes. For V-i curve measurements under each testing condition, potentiodynamic scans starting from open-circuit voltage to both fuel cell (negative) and electrolysis (positive) directions were performed, with voltage scan rate of 10 mV s^{-1}. EIS measurements were performed in the frequency range from 200 kHz to 100 mHz with sinus amplitude of 5 mV, at OCV and also under DC voltage bias of +0.2 V (electrolysis mode) or -0.2 V (fuel cell mode). All electrochemical measurements were made with a multichannel potentio/galvanostat (Biologic VMP3) equipped with power boosters (Biologic VMP3B-5).

Microstructure Characterization: The micron-scale cell structure was observed on a polished cross-section mounted in epoxy using a tabletop scanning electron microscope (SEM, Hitachi TM-1000). The nano-structured catalysts in fractured cell cross section were imaged using the secondary electron detector of a field emission scanning electron microscope (FESEM, Zeiss Gemini Ultra-55) with a beam energy of 5 kV. An EDAX detector was used for energy dispersive X-ray spectroscopy analysis (EDS) with a beam energy of 15 kV.

Supporting Information
Supporting Information is available from the Wiley Online Library or from the author.

Acknowledgements
This work was made possible through the HydroGEN consortium, which was funded by the U.S. Department of Energy, Office of Energy Efficiency and Renewable Energy, Fuel Cell Technologies Office under Award No. DE-EE0008079. The use of Zeiss Gemini Ultra-55 FESEM in the Molecular Foundry of Lawrence Berkeley National Laboratory was supported by the Office of Science, Office of Basic Energy Sciences, of the U.S. Department of Energy under Contract No. DE-AC02-05CH11231. This work was funded in part by the U.S. Department of Energy under contract no. DE-AC02-05CH11231. The views and opinions of the authors expressed herein do not necessarily state or reflect those of the United States Government or any agency thereof. Neither the United States Government nor any agency thereof, nor any of their employees, makes any warranty, expressed or implied, or assumes any legal liability or responsibility for the accuracy, completeness, or usefulness of any information, apparatus, product, or process disclosed, or represents that its use would not infringe privately owned rights.

Received: ((will be filled in by the editorial staff))
Revised: ((will be filled in by the editorial staff))
Published online: ((will be filled in by the editorial staff))

References

[1] G.W. Crabtree, M.S. Dresselhaus, M.V. Buchanan, Physics Today, 57 (2004) 39-44.

[2] J.A. Turner, Science, 305 (2004) 972-974.

[3] G. Marbán, T. Valdés-Solís, International Journal of Hydrogen Energy, 32 (2007) 1625-1637.

[4] H.F. Abbas, W.W. Daud, International Journal of Hydrogen Energy, 35 (2010) 1160-1190.

[5] A.L. Dicks, Journal of Power Sources, 61 (1996) 113-124.

[6] A. Haryanto, S. Fernando, N. Murali, S. Adhikari, Energy & Fuels, 19 (2005) 2098-2106.

[7] R. Kothari, D. Buddhi, R. Sawhney, Renewable and Sustainable Energy Reviews, 12 (2008) 553-563.

[8] M. Carmo, D.L. Fritz, J. Mergel, D. Stolten, International journal of hydrogen energy, 38 (2013) 4901-4934.

[9] M. Ni, M.K. Leung, D.Y. Leung, International Journal of Hydrogen Energy, 33 (2008) 2337-2354.

[10] A. Ursua, L.M. Gandia, P. Sanchis, Proceedings of the IEEE, 100 (2012) 410-426.

[11] K. Zeng, D. Zhang, Progress in Energy and Combustion Science, 36 (2010) 307-326.

[12] S.D. Ebbesen, S.H. Jensen, A. Hauch, M.B. Mogensen, Chemical reviews, 114 (2014) 10697-10734.

[13] J. Laurencin, J. Mougin, High-Temperature Steam Electrolysis, in: A. Godula-Jopek (Ed.) Hydrogen Production: by Electrolysis, Wiley-VCH Verlag GmbH & Co. KGaA, Weinheim, Germany, 2015.

[14] L. Bi, S. Boulfrad, E. Traversa, Chemical Society Reviews, 43 (2014) 8255-8270.

[15] A. Brisse, J. Schefold, M. Zahid, International journal of hydrogen energy, 33 (2008) 5375-5382.

[16] M. Laguna-Bercero, Journal of Power Sources, 203 (2012) 4-16.

[17] J. O'Brien, C. Stoots, J. Herring, P. Lessing, J. Hartvigsen, S. Elangovan, Journal of Fuel Cell Science and Technology, 2 (2005) 156-163.

[18] G. Schiller, A. Ansar, M. Lang, O. Patz, Journal of Applied Electrochemistry, 39 (2009) 293-301.

[19] A.B. Stambouli, E. Traversa, Renewable and sustainable energy reviews, 6 (2002) 433-455.

[20] J.B. Hansen, Faraday discussions, 182 (2015) 9-48.

[21] in, HELMETH.

[22] S.-L. Zhang, H. Wang, M.Y. Lu, A.-P. Zhang, L.V. Mogni, Q. Liu, C.-X. Li, C.-J. Li, S.A. Barnett, Energy & Environmental Science, (2018).

[23] M. Reytier, S. Di Iorio, A. Chatroux, M. Petitjean, J. Cren, M. De Saint Jean, J. Aicart, J. Mougin, International Journal of Hydrogen Energy, 40 (2015) 11370-11377.

[24] J. Mougin, A. Chatroux, K. Couturier, M. Petitjean, M. Reytier, G. Gousseau, F. Lefebvre-Joud, Energy Procedia, 29 (2012) 445-454.

[25] A. Hauch, S.D. Ebbesen, S.H. Jensen, M. Mogensen, Journal of Materials Chemistry, 18 (2008) 2331-2340.

[26] A. Jun, J. Kim, J. Shin, G. Kim, Angewandte Chemie International Edition, 55 (2016) 12512-12515.

[27] Z. Gao, V.Y. Zenou, D. Kennouche, L. Marks, S.A. Barnett, Journal of Materials Chemistry A, 3 (2015) 9955-9964.

[28] Z. Gao, H. Wang, E. Miller, Q. Liu, D. Senn, S. Barnett, ACS applied materials & interfaces, 9 (2017) 7115-7124.

[29] J. Kim, A. Jun, O. Gwon, S. Yoo, M. Liu, J. Shin, T.-H. Lim, G. Kim, Nano Energy, 44 (2018) 121-126.

[30] A. Hauch, K. Brodersen, M. Chen, C. Graves, S.H. Jensen, P.S. Jørgensen, P.V. Hendriksen, M.B. Mogensen, S. Ovtar, X. Sun, ECS Transactions, 75 (2017) 3-14.

[31] C. Yang, Z. Yang, C. Jin, M. Liu, F. Chen, international journal of hydrogen energy, 38 (2013) 11202-11208.

[32] S.H. Jensen, X. Sun, S.D. Ebbesen, R. Knibbe, M. Mogensen, International journal of hydrogen energy, 35 (2010) 9544-9549.

[33] X. Yang, J.T. Irvine, Journal of Materials Chemistry, 18 (2008) 2349-2354.

[34] M. Laguna-Bercero, S. Skinner, J. Kilner, Journal of Power Sources, 192 (2009) 126-131.

[35] Q. Liu, C. Yang, X. Dong, F. Chen, international journal of hydrogen energy, 35 (2010) 10039-10044.

[36] F. Tietz, D. Sebold, A. Brisse, J. Schefold, Journal of Power Sources, 223 (2013) 129-135.

[37] X. Sun, M. Chen, Y.-L. Liu, P. Hjalmarsson, S.D. Ebbesen, S.H. Jensen, M.B. Mogensen, P.V. Hendriksen, Journal of The Electrochemical Society, 160 (2013) F1074-F1080.

[38] N. Zhou, Y.-M. Yin, J. Li, L. Xu, Z.-F. Ma, Journal of Power Sources, 340 (2017) 373-379.

[39] A. Mahmood, S. Bano, J.H. Yu, K.-H. Lee, Energy, 90 (2015) 344-350.

[40] A. Hauch, S. Ebbesen, S.H. Jensen, M. Mogensen, Journal of the Electrochemical Society, 155 (2008) B1184-B1193.

[41] M.C. Tucker, Journal of Power Sources, 195 (2010) 4570-4582.

[42] V.V. Krishnan, Wiley Interdisciplinary Reviews: Energy and Environment, 6 (2017) e246.

[43] Y. Larring, M.-L. Fontaine, Critical issues of metal-supported fuel cell, in: Solid Oxide Fuels Cells: Facts and Figures, Springer, 2013, pp. 71-93.

[44] M.C. Tucker, C.P. Jacobson, L.C. De Jonghe, S.J. Visco, Journal of Power Sources, 160 (2006) 1049-1057.

[45] M.C. Tucker, G.Y. Lau, C.P. Jacobson, L.C. DeJonghe, S.J. Visco, Journal of Power Sources, 171 (2007) 477-482.

[46] M.C. Tucker, G.Y. Lau, C.P. Jacobson, L.C. DeJonghe, S.J. Visco, Journal of Power Sources, 175 (2008) 447-451.

[47] M.C. Tucker, Energy Technology, 5 (2017) 2175-2181.

[48] M.C. Tucker, Journal of Power Sources, 369 (2017) 6-12.

[49] M.C. Tucker, A.S. Ying, International Journal of Hydrogen Energy, 42 (2017) 24426-24434.

[50] M.C. Tucker, Journal of Power Sources, 395 (2018) 314-317.

[51] M.C. Tucker, International Journal of Hydrogen Energy, 43 (2018) 8991-8998.

[52] E. Sarasketa-Zabala, L. Otaegi, L. Rodriguez-Martinez, M. Alvarez, N. Burgos, F. Castro, I. Villarreal, Solid State Ionics, 222 (2012) 16-22.

[53] P. Blennow, J. Hjelm, T. Klemensø, S. Ramousse, A. Kromp, A. Leonide, A. Weber, Journal of Power Sources, 196 (2011) 7117-7125.

[54] P. Blennow, B.R. Sudireddy, Å.H. Persson, T. Klemensø, J. Nielsen, K. Thydén, Fuel Cells, 13 (2013) 494-505.

[55] A. Kromp, J. Nielsen, P. Blennow, T. Klemensø, A. Weber, Fuel Cells, 13 (2013) 598-604.

[56] B.R. Sudireddy, J. Nielsen, Å.H. Persson, K. Thydén, K. Brodersen, S. Ramousse, D. Neagu, E. Stefan, J. Irvine, H. Geisler, Fuel Cells, 17 (2017) 508-516.

[57] J. Nielsen, Å.H. Persson, B.R. Sudireddy, J.T. Irvine, K. Thydén, Journal of Power Sources, 372 (2017) 99-106.

[58] J. Nielsen, Å.H. Persson, T.T. Muhl, K. Brodersen, Journal of The Electrochemical Society, 165 (2018) F90-F96.

[59] R. Reolon, S. Sanna, Y. Xu, I. Lee, C. Bergmann, N. Pryds, V. Esposito, Journal of Materials Chemistry A, 6 (2018) 7887-7896.

[60] M. Haydn, K. Ortner, T. Franco, S. Uhlenbruck, N.H. Menzler, D. Stöver, G. Bräuer, A. Venskutonis, L.S. Sigl, H.-P. Buchkremer, Journal of Power Sources, 256 (2014) 52-60.

[61] D. Udomsilp, D. Roehrens, N. Menzler, C. Bischof, L. de Haart, A. Opitz, O. Guillon, M. Bram, Journal of The Electrochemical Society, 164 (2017) F1375-F1384.

[62] Y. Zhou, H. Wu, T. Luo, J. Wang, Y. Shi, C. Xia, S. Wang, Z. Zhan, Advanced Energy Materials, 5 (2015) 1500375.

[63] S.-F. Yang, C.-S. Hwang, C.-H. Tsai, C.-L. Chang, M.-H. Wu, IEEE Transactions on Plasma Science, 45 (2017) 318-322.

[64] H.C. Pham, S. Taniguchi, Y. Inoue, J. Matsuda, J.T. Chou, Y. Misu, K. Matsuoka, K. Sasaki, Fuel Cells, 17 (2017) 83-89.

[65] C. Lee, J. Bae, Journal of Power Sources, 176 (2008) 62-69.

[66] A. Ansar, P. Szabo, J. Arnold, Z. Ilhan, D. Soysal, R. Costa, A. Zagst, M. Gindrat, T. Franco, Ecs Transactions, 35 (2011) 147-155.

[67] Y. Zhou, X. Xin, J. Li, X. Ye, C. Xia, S. Wang, Z. Zhan, international journal of hydrogen energy, 39 (2014) 2279-2285.

[68] Y. Zhou, C. Yuan, T. Chen, X. Meng, X. Ye, J. Li, S. Wang, Z. Zhan, Journal of Power Sources, 267 (2014) 117-122.

[69] A. Macwan, D. Chen, M. Marr, O. Kesler, Journal of Power Sources, 221 (2013) 397-405.

[70] B.J. McKenna, N. Christiansen, R. Schauperl, P. Prenninger, J. Nielsen, P. Blennow, T. Klemensø, S. Ramousse, A. Kromp, A. Weber, Fuel cells, 13 (2013) 592-597.

[71] R.T. Leah, A. Bone, M. Lankin, A. Selcuk, M. Rahman, A. Clare, L. Rees, S. Phillip, S. Mukerjee, M. Selby, ECS Transactions, 68 (2015) 95-107.

[72] A. Nechache, F. Han, R. Semerad, G. Schiller, R. Costa, ECS Transactions, 78 (2017) 3039-3047.

[73] T. Chen, Y. Zhou, M. Liu, C. Yuan, X. Ye, Z. Zhan, S. Wang, Electrochemistry Communications, 54 (2015) 23-27.

[74] C. Nicollet, A. Flura, V. Vibhu, A. Rougier, J.-M. Bassat, J.-C. Grenier, international journal of hydrogen energy, 41 (2016) 15538-15544.

[75] R. Sharma, E. Djurado, Journal of Materials Chemistry A, (2018).

[76] V. Thangadurai, R.A. Huggins, W. Weppner, Journal of Solid State Electrochemistry, 5 (2001) 531-537.

[77] S. Ferro, International Journal of Electrochemistry, 2011 (2011).

[78] B. Fan, J. Yan, X. Yan, Solid State Sciences, 13 (2011) 1835-1839.

[79] D. Ding, X. Li, S.Y. Lai, K. Gerdes, M. Liu, Energy & Environmental Science, 7 (2014) 552-575.

[80] D. Ding, M. Gong, C. Xu, N. Baxter, Y. Li, J. Zondlo, K. Gerdes, X. Liu, Journal of Power Sources, 196 (2011) 2551-2557.

[81] S. Zhu, D. Ding, M. Li, C. Xia, Journal of The Electrochemical Society, 164 (2017) F916-F922.

[82] T. Wang, C. Sun, F. Zhen, W. Song, R. Li, Q. Zhen, Fuel Cells, 16 (2016) 611-616.

[83] S.P. Jiang, International journal of hydrogen energy, 37 (2012) 449-470.

[84] K. Chen, N. Ai, S.P. Jiang, International Journal of Hydrogen Energy, 39 (2014) 10349-10358.

[85] A.R. Hanifi, M. Laguna-Bercero, T.H. Etsell, P. Sarkar, International Journal of Hydrogen Energy, 39 (2014) 8002-8008.

[86] H. Schichlein, A.C. Müller, M. Voigts, A. Krügel, E. Ivers-Tiffée, Journal of Applied Electrochemistry, 32 (2002) 875-882.

[87] A. Leonide, V. Sonn, A. Weber, E. Ivers-Tiffée, Journal of The Electrochemical Society, 155 (2008) B36-B41.

[88] C. Graves, S.D. Ebbesen, M. Mogensen, Solid State Ionics, 192 (2011) 398-403.

[89] Q. Fang, L. Blum, N.H. Menzler, Journal of The Electrochemical Society, 162 (2015) F907-F912.

[90] J. Yan, H. Chen, E. Dogdibegovic, J.W. Stevenson, M. Cheng, X.-D. Zhou, Journal of Power Sources, 252 (2014) 79-84.

[91] H. Sumi, H. Shimada, Y. Yamaguchi, T. Yamaguchi, Journal of The Electrochemical Society, 164 (2017) F243-F247.

[92] H. Sumi, D. Kennouche, K. Yakal-Kremski, T. Suzuki, S.A. Barnett, D.J. Miller, T. Yamaguchi, K. Hamamoto, Y. Fujishiro, Solid State Ionics, 285 (2016) 227-233.

[93] Y. Chen, Y. Choi, S. Yoo, Y. Ding, R. Yan, K. Pei, C. Qu, L. Zhang, I. Chang, B. Zhao, Joule, 2 (2018) 938-949.

[94] T.H. Wan, M. Saccoccio, C. Chen, F. Ciucci, Electrochimica Acta, 184 (2015) 483-499.

[95] B.A. Boukamp, A. Rolle, Solid state ionics, 314 (2018) 103-111.

[96] M. Kornely, A. Neumann, N.H. Menzler, A. Leonide, A. Weber, E. Ivers-Tiffée, Journal of Power Sources, 196 (2011) 7203-7208.

[97] V. Sonn, A. Leonide, E. Ivers-Tiffée, Journal of The Electrochemical Society, 155 (2008) B675-B679.

[98] Y. Yan, Q. Fang, L. Blum, W. Lehnert, Electrochimica Acta, 258 (2017) 1254-1261.

[99] F. Chauveau, J. Mougin, J.-M. Bassat, F. Mauvy, J.-C. Grenier, Journal of Power Sources, 195 (2010) 744-749.

[100] E. Dogdibegovic, R. Wang, G.Y. Lau, M.C. Tucker, Journal of Power Sources, under review (2018).

[101] L. Bi, S.P. Shafi, E. Traversa, Journal of Materials Chemistry A, 3 (2015) 5815-5819.

[102] L. Lei, Z. Tao, X. Wang, J.P. Lemmon, F. Chen, Journal of Materials Chemistry A, 5 (2017) 22945-22951.

[103] W. Wu, H. Ding, Y. Zhang, Y. Ding, P. Katiyar, P.K. Majumdar, T. He, D. Ding, Advanced Science, (2018) 1800360.

[104] T.Z. Sholklapper, V. Radmilovic, C.P. Jacobson, S.J. Visco, L.C. De Jonghe, Electrochemical and solid-state letters, 10 (2007) B74-B76.

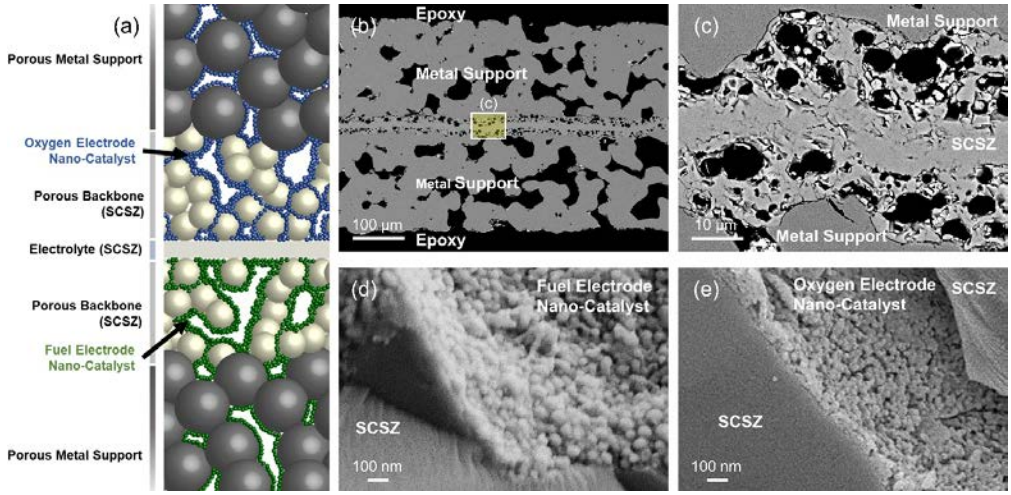

Figure 1. Cell structure. (a) Schematic of the MS-SOEC microstructure. (b) SEM micrographs of the cross-section of the MS-SOEC showing the "metal-support/SCSZ backbone/SCSZ dense electrolyte/SCSZ backbone/metal-support" symmetric structure. (c) Cross-section of porous backbones and dense electrolyte, (d) hydrogen electrode catalyst (Ni-SDC) infiltrated on SCSZ backbone, (e) oxygen electrode catalyst (Pr_6O_{11}) infiltrated on SCSZ backbone.

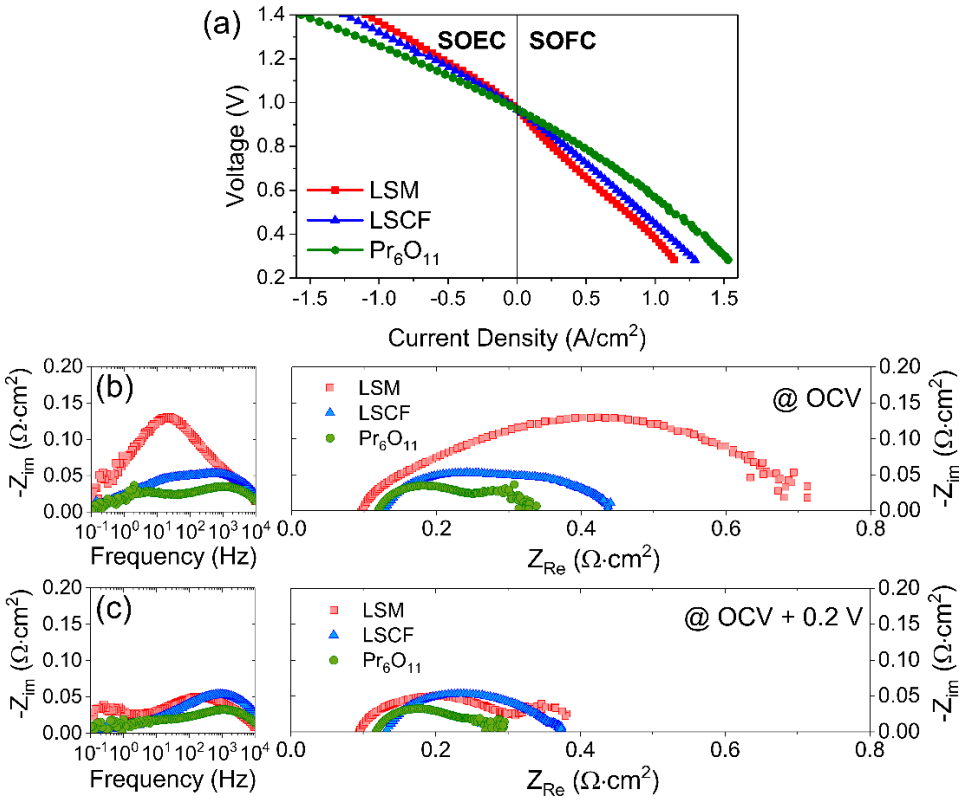

Figure 2. Impact of oxygen electrocatalyst composition on performance. (a) Voltage - current density curves of MS-SOC operated under both electrolysis and fuel cell modes at 700 °C and 50 vol.% steam, with LSM, LSCF, or Pr_6O_{11} as oxygen electrode catalysts and SDCN20 as hydrogen electrode catalyst. (b, c) Bode and Nyquist impedance spectra at (b) OCV, and (c) OCV + 0.2 V.

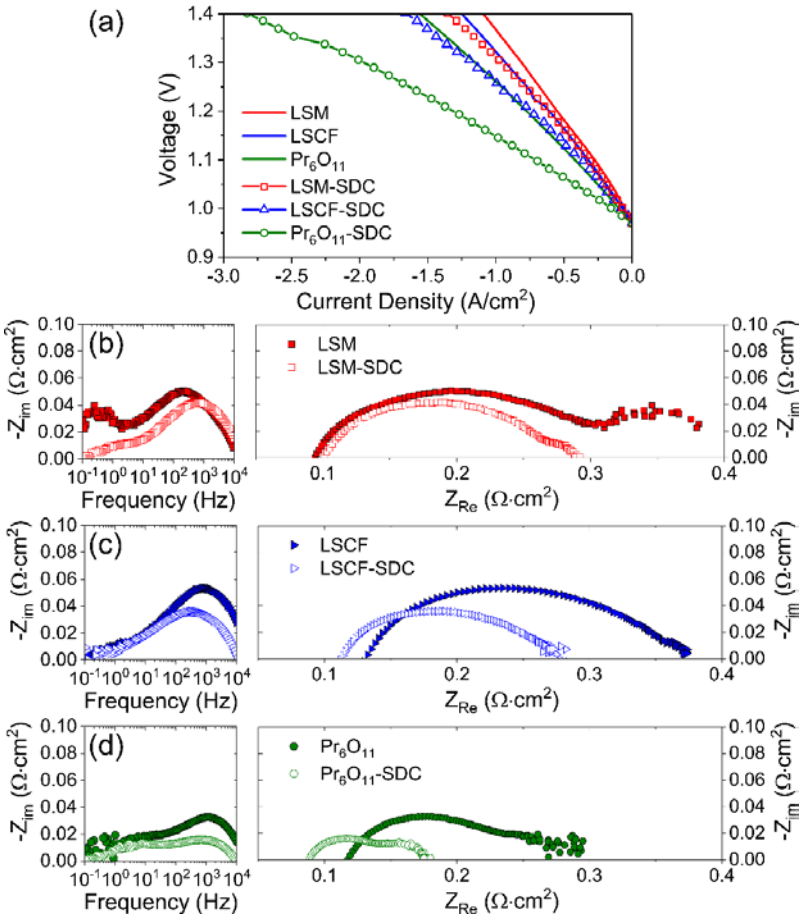

Figure 3. Impact of adding SDC to the oxygen electrode. (a) Voltage - current density curves of MS-SOECs, comparing composite catalysts (LSM-SDC, LSCF-SDC and Pr_6O_{11}-SDC) with single catalysts (LSM, LSCF and Pr_6O_{11}) in oxygen electrode. (b, c, d) Bode and Nyquist impedance spectra at + 0.2 V bias for (b) LSM and LSM-SDC, (c) LSCF and LSCF-SDC, (d) Pr_6O_{11} and Pr_6O_{11}-SDC catalysts. All cells had SDCN20 as hydrogen electrode catalyst and were operated at 700 °C and 50 vol.% steam content.

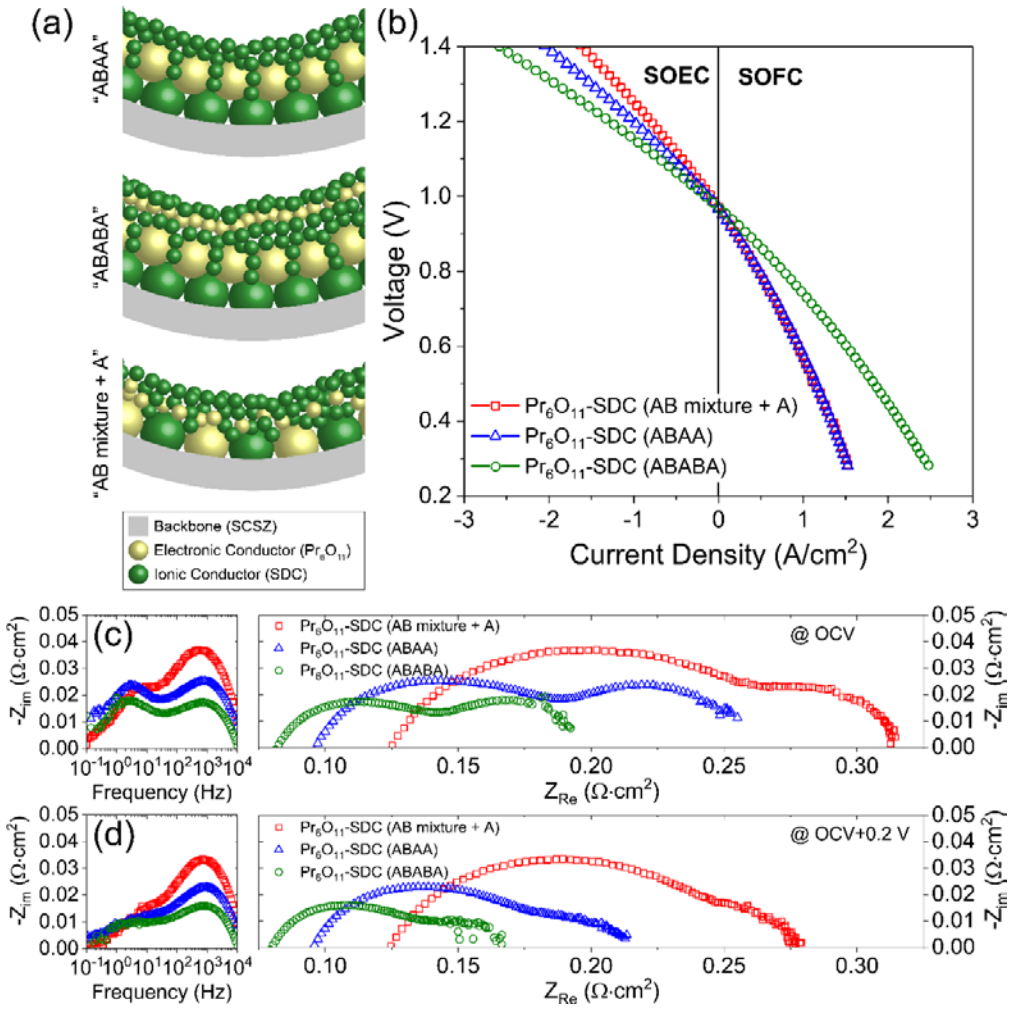

Figure 4. Influence of composite Pr_6O_{11}-SDC multi-layer deposition sequence. (a) Schematics of composite oxygen electrode catalyst in a pore within the SCSZ backbone, with "ABAA", "ABABA", and "ABmix+A" sequences (A = Pr_6O_{11}, B = SDC). Larger and smaller particle size represents the catalysts fired at 850 °C and 600 °C, respectively, and do not necessarily correlate to their actual size ratio. (b) Voltage - current density curves of MS-SOC operated under both electrolysis and fuel cell mode with the various sequences of composite oxygen electrode. (c, d) Corresponding Bode and Nyquist plots of cell impedances measured at (c) OCV and (d) + 0.2 V bias. All cells had SDCN20 as hydrogen electrode catalyst and were operated at 700 °C and 50 vol.% steam content.

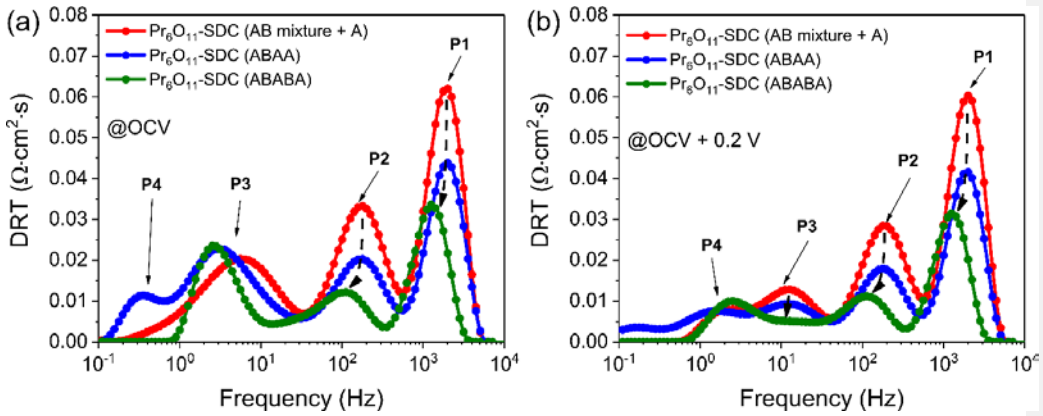

Figure 5. Distribution of relaxation times (DRT) analysis of cells infiltrated with various catalyst sequences for impedance measured (a) at OCV, (b) at +0.2 V DC bias.

Comment [MCT1]: X-axis positions of the dat seems to have changed compared to earlier versio Please check…It may just be a label error.

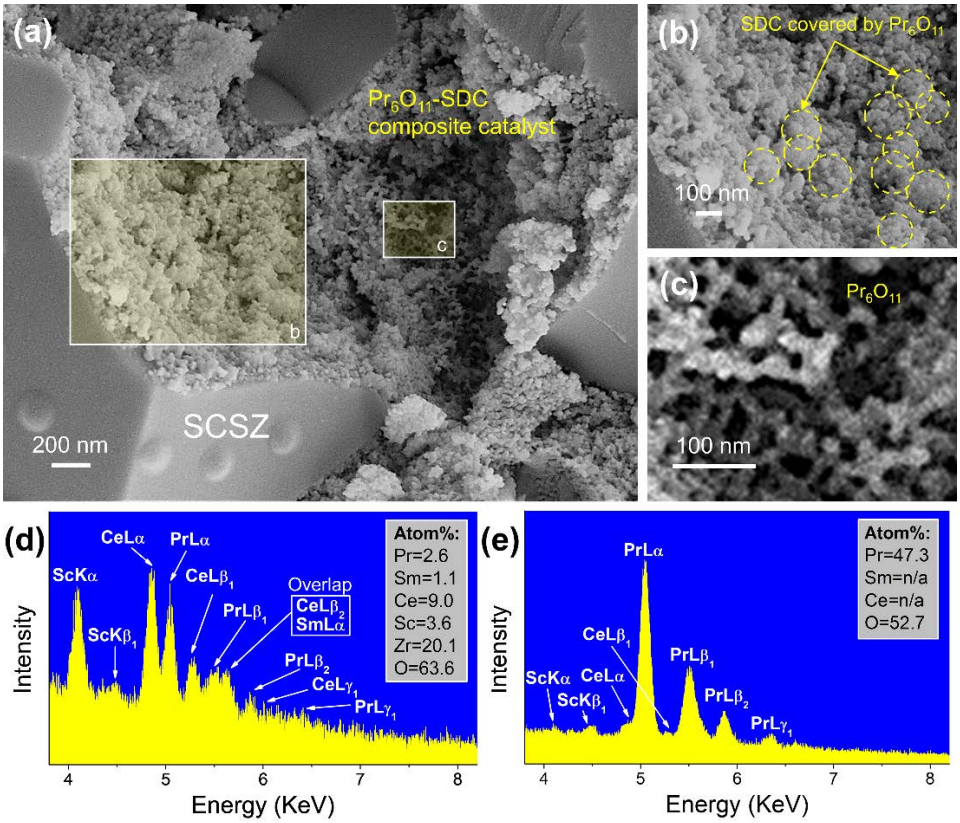

Figure 6. Nanostructure of ABABA composite oxygen catalyst. (a) Pr_6O_{11}-SDC composite calcined catalyst in the fractured porous SCSZ backbone infiltrated with alternating-layer catalyst infiltration sequence. (b) Area showing SDC covered by Pr_6O_{11} particles. (c) Area showing Pr_6O_{11} particles. (d) EDS spectrum from (b) showing mixture of Pr_6O_{11} and SDC. (e) EDS spectrum from (c) showing pure Pr_6O_{11}.

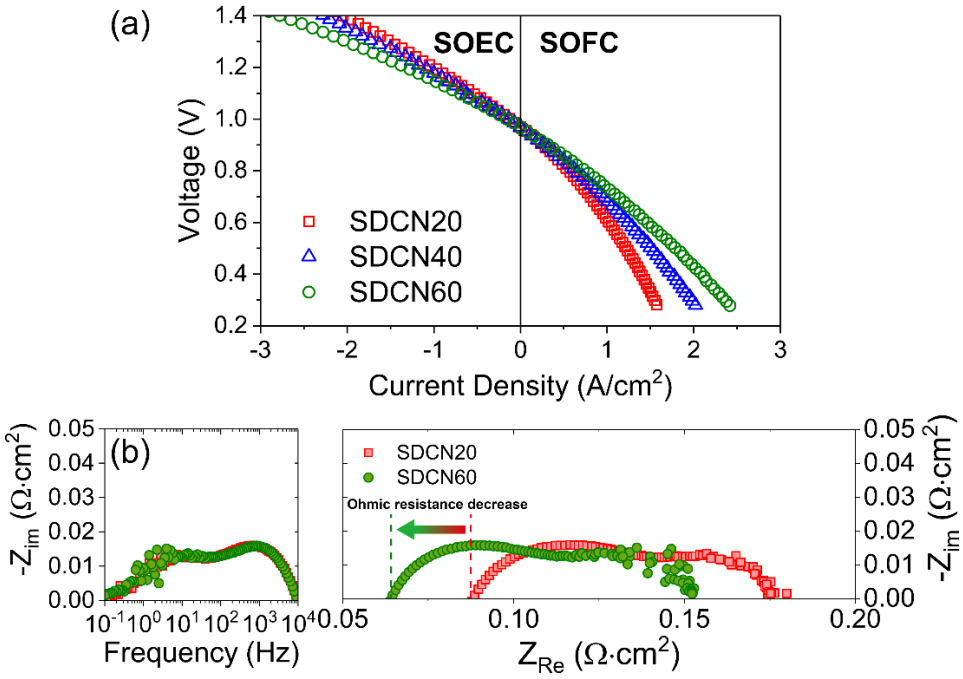

Figure 7. Impact of Ni:SDC ratio in hydrogen electrode. (a) Voltage - current density curves of MS-SOC operated under both electrolysis and fuel cell modewith 20, 40, and 60 vol.% of Ni (i.e. SDCN20, SDCN40, and SDCN60) in Ni-SDC as hydrogen electrode catalysts. (b) Bode and Nyquist impedance spectra at + 0.2 V bias for cells with 20 and 60 vol.% of Ni in Ni-SDC (i.e. SDCN20 and SDCN60). All cells had Pr_6O_{11}-SDC as oxygen electrode catalyst and were operated at 700 °C and 50 vol.% steam content.

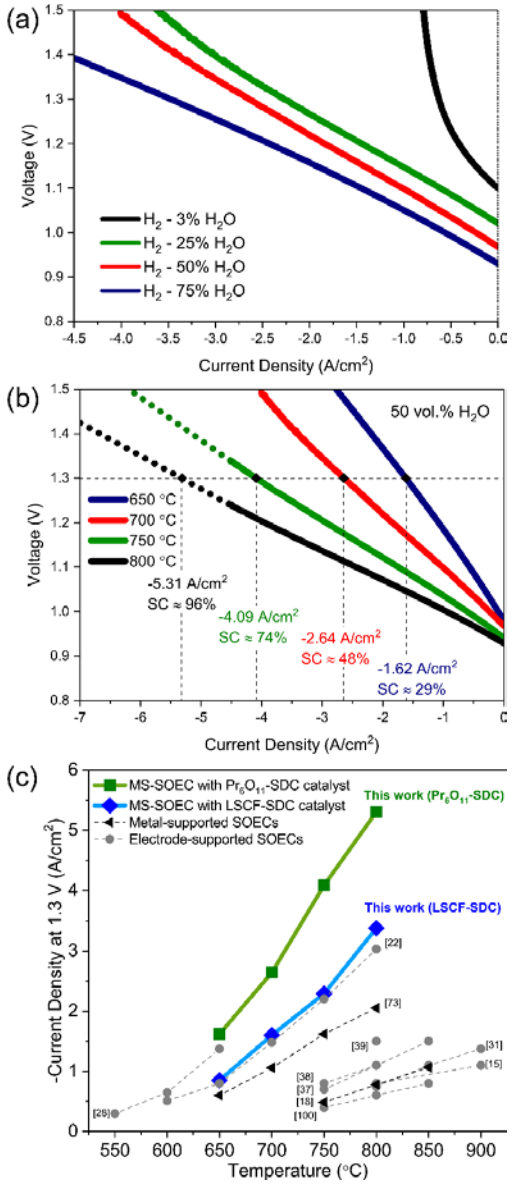

Figure 8. Performance of optimized cell with Pr_6O_{11}-SDC as oxygen electrode catalyst and SDCN60 as hydrogen electrode. (a) Influence of steam content in the hydrogen supply on electrolysis and fuel cell polarization at 700 °C. (b) Influence of temperature on the electrolysis polarization at 50 vol.% H_2O (V-i curves for 750 and 800 °C were extrapolated due to instrument limitation). Corresponding current densities and steam-to-hydrogen conversion rates (SC) at 1.3 V are displayed. (c) Comparison of electrolysis performance of optimized cells with Pr_6O_{11}-SDC and LSCF-SDC to literature data for conventional electrode-supported and metal-supported SOECs based on oxygen conductors (such as stabilized-zirconia and lanthanum strontium gallate magnesite) [15, 18, 22, 28, 31, 37-39, 73, 99].

Copyright WILEY-VCH Verlag GmbH & Co. KGaA, 69469 Weinheim, Germany, 2016.

Supporting Information

Metal-Supported Solid Oxide Electrolysis Cell (MS-SOEC) With Significantly Enhanced Catalysis

*Ruofan Wang, Emir Dogdibegovic, Grace Y. Lau, Michael C. Tucker**

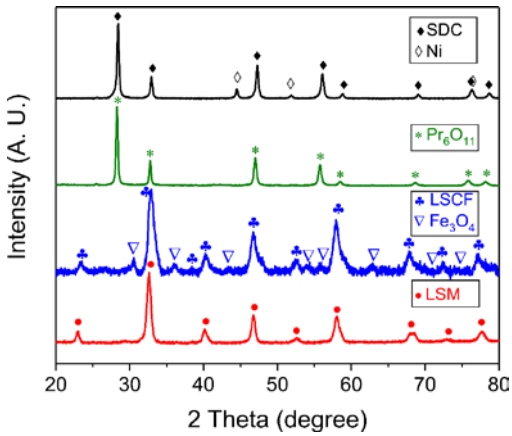

Figure S1. X-ray diffraction patterns of LSM, LSCF, Pr_6O_{11}, and SDC with 20 vol.% Ni, obtained by calcining corresponding precursor solutions of nitrate salts at 700 °C for 1 h. SDC with 20 vol.% Ni was obtained by reducing SDC-NiO mixture at 700 °C for 1 h after calcination. Fe_3O_4 impurity was found to be formed together with LSCF. XRD patterns were collected using a Bruker D2 PHASER X-ray diffractometer with CuKα radiation.

Supplementary Note 1. Symmetric cell study

In addition to full cells, fully symmetric cells with identical LSCF-SDC, Pr_6O_{11}-SDC or SDCN20 catalyst on both sides were fabricated. The cells with different symmetric catalysts were tested in their corresponding atmospheres (i.e. Pr_6O_{11}-SDC and LSCF-SDC symmetric cells in ambient air and SDCN symmetric cell in humidified hydrogen), and their impedance spectra were measured at OCV. The intention here was to compare the magnitudes of different electrode resistances.

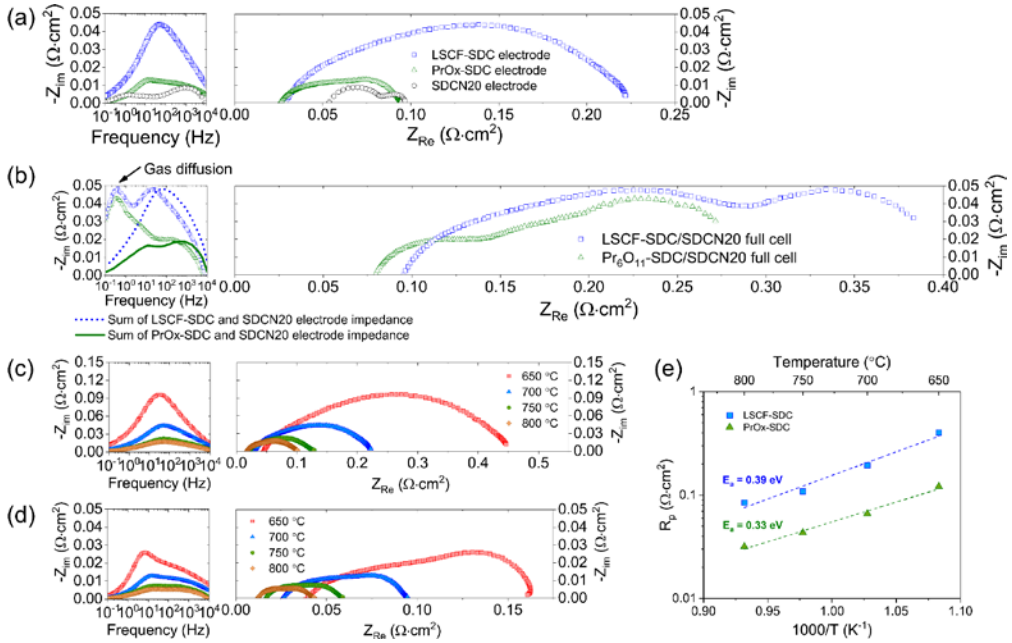

Figure S2. (a) Bode and Nyquist plots of symmetric cells with same catalyst (LSCF-SDC, or Pr_6O_{11}-SDC, or SDCN20) infiltrated on both sides, measured at OCV and 700 °C. LSCF-SDC and Pr_6O_{11}-SDC symmetric cells were tested in ambient air, and SDCN20 symmetric cell was tested in 3% humidified hydrogen with 50 sccm flow rate. The measured impedance was divided by two, and the single electrode resistance was obtained and presented in the figure. (b) Bode and Nyquist plots of full cells with LSCF-SDC and Pr_6O_{11}-SDC as oxygen electrode (exposed to ambient air), and SDCN20 as hydrogen electrode (exposed to 3% humidified hydrogen with 50 sccm flow rate), measured at OCV and 700 °C. Dashed lines in Bode plot display the sum of LSCF-SDC and SDCN20 and the sum of Pr_6O_{11}-SDC and SDCN20 electrode impedances obtained from symmetric cell testing. (c, d) Impedance spectra as a function of temperature of (c) LSCF-SDC electrode, and (d) Pr_6O_{11}-SDC electrode. (e) Arrhenius plots for LSCF-SDC and Pr_6O_{11}-SDC electrode vs reciprocal temperature.

Fig. S2a shows the impedance spectra of symmetric cells at 700 °C with LSCF-SDC, Pr_6O_{11}-SDC, and SDCN20 catalysts, showing polarization resistance (R_p) of 0.19, 0.07, and 0.04 $\Omega \cdot cm^2$ respectively. Compared to LSCF-SDC electrode, Pr_6O_{11}-SDC electrode provided a much smaller R_p, which corresponded to the better full cell performance with such oxygen electrode. However, when comparing oxygen electrode to hydrogen electrode, it is obvious that oxygen electrode had a higher polarization resistance, indicating R_p from oxygen electrode was still dominant in full cell. On the other hand, hydrogen electrode SDCN20 appeared to have a larger ohmic resistance than both LSCF-SDC and Pr_6O_{11}-SDC oxygen electrode.

Fig. S2b shows the Bode and Nyquist plots of cells with LSCF-SDC and Pr_6O_{11}-SDC as oxygen electrodes and SDCN20 as hydrogen electrode, measured under OCV, at 700 °C and 3 vol.% H_2O on the hydrogen electrode side. The sums of oxygen and hydrogen electrode impedances on the frequency domain (i.e. $-(Z_{im,LSCF\text{-}SDC}+Z_{im,SDCN20})$, and $-(Z_{im,Pr6O11\text{-}SDC}+Z_{im,SDCN20})$) are also shown as dashed lines in the Bode plot of Fig. S2b. Compared to Bode plots from full cell measurements, the sums of electrode impedances from symmetric cells show similar magnitude at higher frequencies ($10^2 - 10^4$ Hz), indicating that the processes in this frequency range (typically including charge transfer and oxygen surface exchange/O^{2-} bulk diffusion) can be well detected by symmetric cell measurement. However, the gas diffusion process occurred at low frequencies (10^{-1} - 10 Hz) was almost not detected in symmetric cell testing, because the oxygen partial pressure difference in the symmetric cell electrodes was much smaller than that in full cell electrodes.

Figures S2c-S2e show the impedance spectra and electrode polarizations as a function of temperature for LSCF-SDC and Pr_6O_{11}-SDC electrodes. Pr_6O_{11}-SDC electrode showed much smaller electrode resistance than LSCF-SDC electrode at the same temperature. The

activation energies for LSCF-SDC and Pr_6O_{11}-SDC electrodes were calculated to be 0.39 and 0.33 eV.

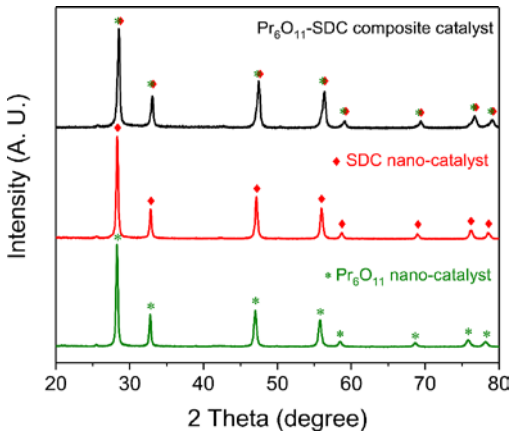

Figure S3. X-ray diffraction patterns of (a) Pr_6O_{11}, SDC, and Pr_6O_{11}-SDC (50:50 vol.%), obtained by calcining corresponding precursor solutions of nitrate salts at 700 °C for 1 h. XRD of the mixed Pr_6O_{11}-SDC confirmed that secondary non-fluorite phases were not formed.

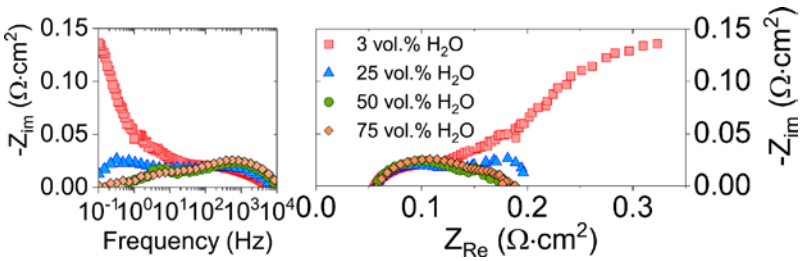

Figure S4. Influence of steam content on impedance spectra. Bode and Nyquist plots of a cell with Pr_6O_{11}-SDC catalyst at 700 °C and with + 0.2 V DC bias, measured with different steam contents over the hydrogen electrode: 3, 25, 50, and 75 vol.% H_2O mixed with H_2. (H_2 flow rate was fixed at 50 sccm, and the corresponding flow rates for H_2O were approximately 1.55, 16.7, 50 and 150 sccm.)

Supplementary Note 2. Effect of Over-Filling with Oxygen Electrode Catalyst

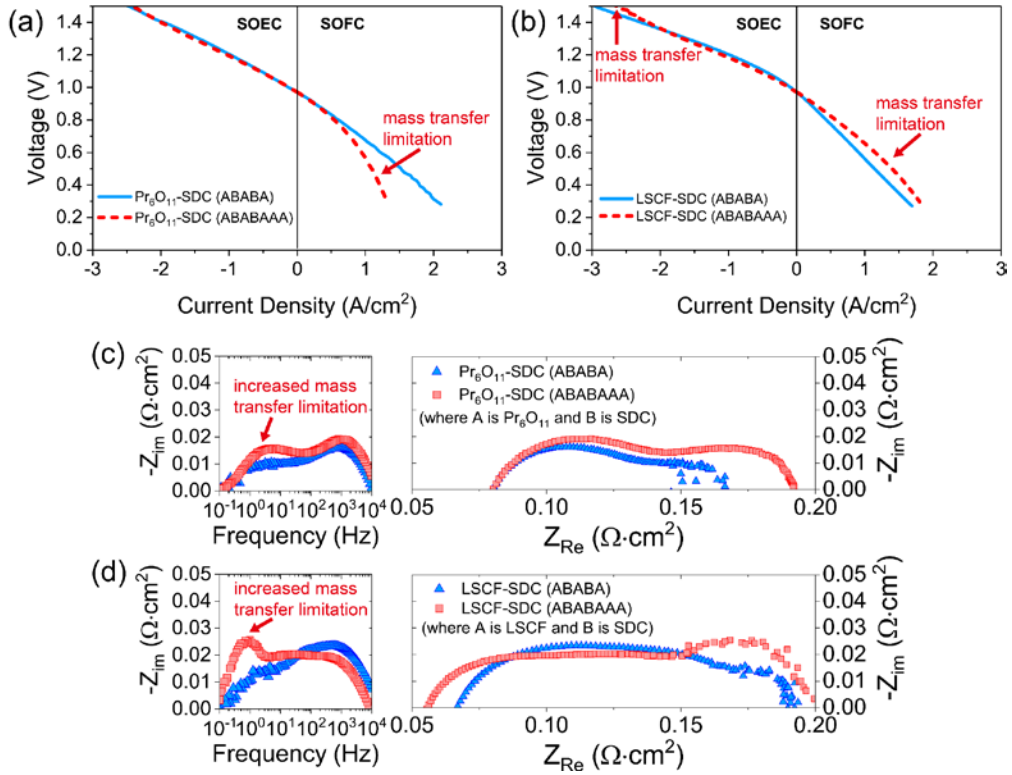

Figure S5. Effect of over-filling the oxygen electrode with catalyst on cell performance. (a, b) Comparison of V-i curves of cells with and without two more infiltration cycles of electronic conductor in oxygen electrode (i.e. "ABABA" vs "ABABAAA") measured at 700 °C and 50 vol.% steam, with (a) Pr_6O_{11}-SDC catalysts, and (b) LSCF-SDC catalysts. (c, d) Bode and Nyquist plots of cells with and without two more infiltration cycles of electronic conductor in oxygen electrode measured at 700 °C and 50 vol.% steam, with (c) Pr_6O_{11}-SDC catalysts, and (d) LSCF-SDC catalysts.

With the impression that a thicker infiltrated nanoparticle-blanket could result in a smaller ohmic resistance (see Fig. 4 in main text), the following question arose: will more infiltration cycles on top of "ABABA" arrangement provide higher cell performance? To answer this question, two more layers of electronic conductors were infiltrated on top of ABABA-infiltrated electrode (denoted as "ABABAAA" arrangement), and the corresponding performances were compared. Both Pr_6O_{11}-SDC and LSCF-SDC composite electrode were investigated here. Fig. S5 compares the performance of Pr_6O_{11}-SDC (Fig. S5a and Fig. S5c) and LSCF-SDC cells (Fig. S5b and Fig. S5d), with and without two additional infiltration

cycles in the oxygen electrode. For both Pr_6O_{11}-SDC and LSCF-SDC cells with additional infiltration cycles, no significant change was found in electrolysis performance. Instead, mass-transfer polarization behaviors in fuel cell mode were observed. Additional infiltration increased the polarization resistance of the cell (Fig. S5c and Fig. S5d). Larger impedance was observed at lower frequency range (10^{-1}-10 Hz), indicating pronounced mass-transport limitation. Therefore, additional infiltration cycles are considered to be detrimental as they may provide over-filling of catalyst in the electrode resulting in pore clogging.

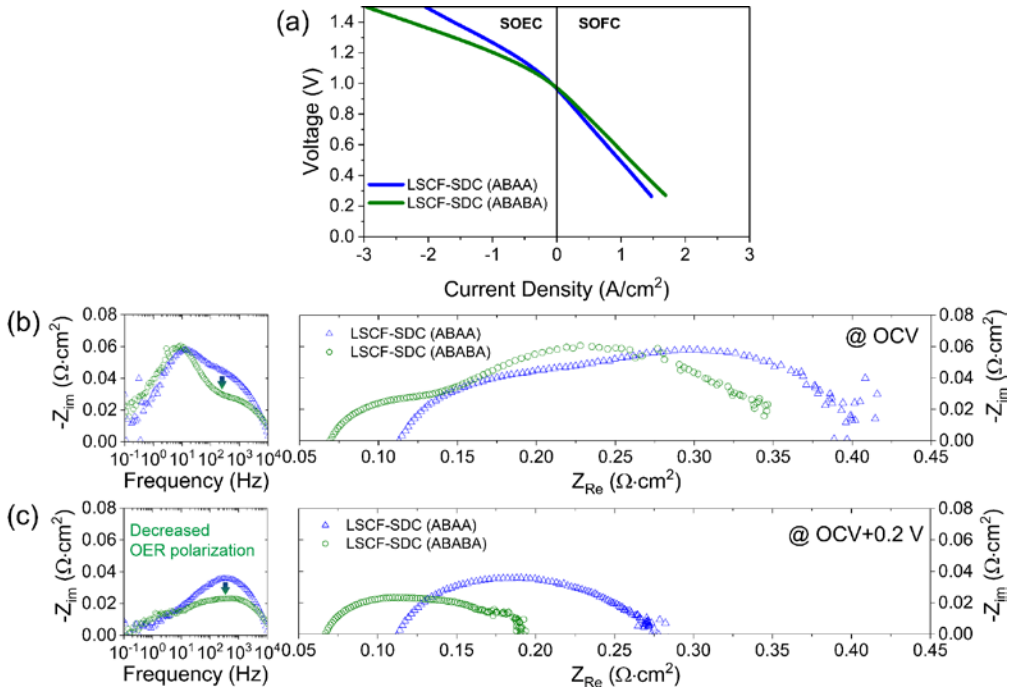

Figure S6. Influence of composite LSCF-SDC multi-layer deposition sequence. (a) Voltage - current density curves of LSCF-SDC based cells with ABAA and ABABA infiltration sequences in oxygen electrode, measured at 700 °C and 50 vol.% H_2O. (b, c) Bode and Nyquist plots of LSCF-SDC based cells with ABAA and ABABA infiltration sequences in oxygen electrode at 700 °C and 50 vol.% steam, measured at (b) OCV, and (c) OCV + 0.2 V. Compared with ABAA infiltrated cell, cell with ABABA infiltration sequence showed reduced impedance at higher frequency, indicating that charge transfer process and/or oxygen exchange/ion diffusion process were improved. Such catalytic improvement was also evident for Pr_6O_{11}-SDC with ABABA infiltration, which therefore confirms the advantage of alternating-layer composite electrode infiltration.

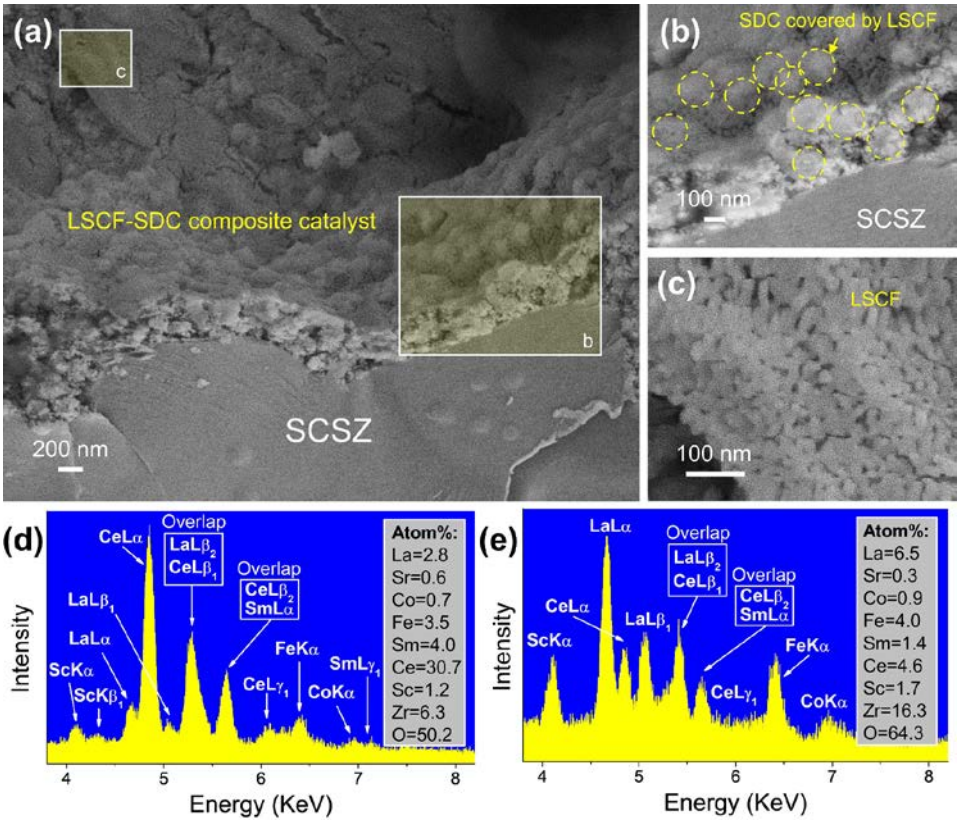

Figure S7. Nanostructure of LSCF-SDC composite catalyst. (a) LSCF-SDC composite calcined catalyst in the fractured porous SCSZ backbone infiltrated with alternating-layer catalyst infiltration sequence. The thickness of the catalyst layer is ~ 300-400 nm for LSCF-SDC. (b) Area showing SDC covered by LSCF particles, where the sizes of SDC particles are ~ 100-150 nm (similar to those SDC particles in the case of Pr_6O_{11}-SDC catalyst). (b) Area showing LSCF particles on the surface of LSCF-SDC electrode, where the particle size of LSCF is ~ 20-30 nm. (d) EDS spectrum from (b). (e) EDS spectrum from (c).

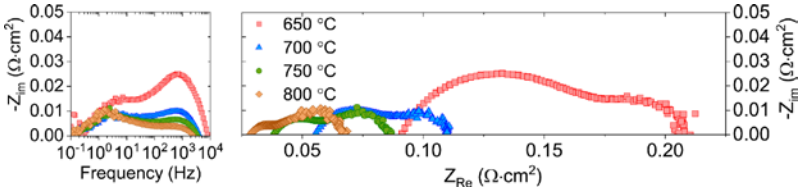

Figure S8. Influence of operating temperature on impedance spectra. Bode and Nyquist plots of the cell with Pr_6O_{11}-SDC catalyst with 50 vol.% H_2O at OCV + 0.2 V (SOEC mode), measured at different temperatures (650, 700, 750, and 800 °C). It was found that the lower frequency process (which is typically associated with gas diffusion or gas conversion) was almost temperature independent, and the processes at intermediate and higher frequencies decreased with increasing temperature.

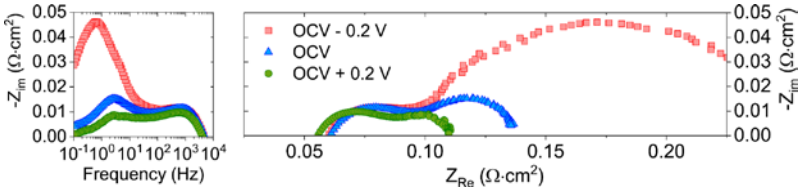

Figure S9. Influence of operating voltage on impedance spectra. Bode and Nyquist plots of the cell with Pr_6O_{11}-SDC catalyst with 50 vol.% H_2O at 700 °C, measured at different DC voltage biases: OCV – 0.2 V (fuel cell mode), OCV, and OCV + 0.2 V (electrolysis mode). It was found that the processes at high frequency (10^3 – 10^4 Hz) and intermediate frequency (10^2 – 10^3 Hz) were almost independent on operating voltage. However, processes at lower frequencies (which are dominated by gas diffusion or gas conversion) diminished when the cell was operated in SOEC mode, but became more pronounced when the cell voltage went more negative (OCV or SOFC mode). Under the specific testing condition of the cell (at 700 °C and with 50 vol.% H_2O in this case), SOEC operation is less resistive mainly because impedance from gas diffusion or conversion in SOEC mode is smaller than in SOFC mode.

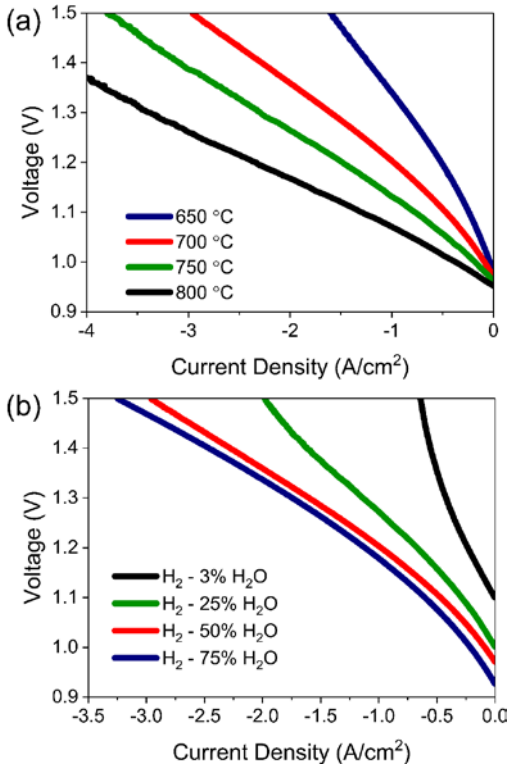

Figure S10. Performance of optimized cell with LSCF-SDC as oxygen electrode catalyst and SDCN60 as hydrogen electrode. (a) Influence of temperature on the electrolysis polarization. At 1.3 V with 50 vol.% steam content, the optimized LSCF-SDC based cell has current densities of -3.38, -2.29, -1.60, and -0.85 A/cm^2 at 800, 750, 700, and 600 °C, respectively. (b) Influence of steam content in the hydrogen supply on electrolysis and fuel cell polarization at 700 °C.

Supplementary Note 3. Calculations of Hydrogen Production Rate and Steam-to-Hydrogen Conversion Rate (SC)

Assuming 100% current efficiency, the hydrogen production rate can be related to the current density passing through the cell using Faraday's law. The molar amount of hydrogen produced per unit time $\dot{n}$ (mol/s) can be expressed as:

$$\dot{n} = \frac{IA}{nF} \quad \text{(Equation S1)}$$

where I is the current density (A/cm^2), A is the active area of the electrolysis cell (cm^2), n is the numbers of electrons transferred per hydrogen molecule produced, and F is the Faraday's constant (C/mol).

The outlet hydrogen flow rate N_{H_2} (sccm) at standard temperature and pressure can thus be expressed as:

$$N_{H_2} = 60 \times 10^3 \times \frac{IAV_{std}}{nF} \quad \text{(Equation S2)}$$

where V_{std} (L/mol) is the volume of 1 mol gas at standard temperature and pressure.

Hydrogen production rate R_{HP} (Nml·cm^{-2}·h^{-1}) can be calculated as:

$$R_{HP} = 60 \times \frac{N_{H_2}}{A} \quad \text{(Equation S3)}$$

The steam-to-hydrogen conversion rate (SC) is calculated as the molar amount of hydrogen produced in the outlet divided by the molar amount of water in the inlet gas:

$$SC = 60 \times \frac{yiRT_{H_2O}}{pN_{H_2O}}$$ (Equation S4)

where R is gas constant ($cm^3 \cdot atm \cdot K^{-1} \cdot mol^{-1}$), T_{H_2O} is the temperature of inlet steam (K), p is the pressure of inlet steam (atm), N_{H_2O} is the flow rate of inlet steam (sccm).

At 1.3 V and 50 vol.% steam content (flow rate of H_2O was 50 sccm at T_{H_2O}=355.15 K), the current densities of our optimized cell were measured to be -5.31, -4.09, -2.64, and -1.62 A/cm^2, at 800, 750, 700, and 600 °C, respectively. The hydrogen production rate and steam-to-hydrogen conversion rate are calculated and listed in Table S1.

Table S1. Hydrogen production rate and steam-to-hydrogen conversion rate (SC) at different temperatures, of optimized cell with Pr_6O_{11}-SDC oxygen electrode and SDCN20 hydrogen electrode (measured at 1.3 V and with 50 sccm of H_2O).

Temperature (°C)	Current density at 1.3 V (A/cm^2)	Outlet hydrogen flow rate (sccm)	Hydrogen production rate ($Nml\ cm^{-2}\ h^{-1}$)	Steam-to-hydrogen conversion rate
800	-5.31	37.0	2219	96%
750	-4.09	28.5	1709	74%
700	-2.64	18.4	1103	48%
650	-1.62	11.3	677	29%